Fizika Nizkikh Temperatur, 2006, v. 32, No. 11, p. 1297–1319

Spectroscopy of atomic and molecular defects in solid ^{4}He using optical, microwave, radio frequency, magnetic and electric fields

(Review Article)

P. Moroshkin, A. Hofer, S. Ulzega, and A. Weis

Physics Department, Université de Fribourg, Chemin du Musée 3, 1700 Fribourg, Switzerland
E-mail: antoine.weis@unifr.ch

Received July 7, 2006, revised July 28, 2006

A little more than a decade ago our team extended the field of defect spectroscopy in cryocrystals to solid ^{4}He matrices, in both their body-centered cubic (bcc) and hexagonally close-packed (hcp) configurations. In this review paper we survey our pioneering activities in the field and compare our results to those obtained in the related fields of doped superfluid helium and doped helium nanodroplets, domains developed in parallel to our own efforts. We present experimental details of the sample preparation and the different spectroscopic techniques. Experimental results of purely optical spectroscopic studies in atoms, exciplexes, and dimers and their interpretation in terms of the so-called bubble model will be discussed. A large part of the paper is devoted to optically detected magnetic resonance, ODMR, processes in alkali atoms. The quantum nature of the helium matrix and the highly isotropic shape of the local trapping sites in the bcc phase make solid helium crystals ideal matrices for high resolution spin physics experiments. We have investigated the matrix effects on both Zeeman and hyperfine magnetic resonance transitions and used ODMR to measure the forbidden electric tensor polarizability in the ground state of cesium. Several unexpected changes of the optical and spin properties during the bcc – hcp phase transition can be explained in terms of small bubble deformations.

PACS: **32.30.–r**, **32.60.+i**, **33.35.+r**, **33.50.–j**, **67.80.–s**, 76.70.Hb

Keywords: cryocrystals, quantum solids, matrix isolation spectroscopy, solid He, exiplexes, atomic bubbles, dimers, optical detected magnetic resonance, Stark effect.

1. Introduction

Since the 1950's, chemists have used solid noble gases or solid nitrogen matrices, so-called cryocrystals for the study of trapped unstable or reactive species, such as free radicals. The technique has become known under the name of matrix isolation spectroscopy (MIS). Solid helium matrix isolation spectroscopy (sHeMIS) described here, is an extension of that field to solid matrices of ^{4}He. This field has emerged from the spectroscopy of point defects in superfluid ^{4}He (He II), studied first with electrons and He ions, and later with atoms and other atomic ions. Historical aspects of defect spectroscopy in liquid and solid helium were reviewed in [1,2]. Several prominent aspects of sHeMIS are intimately related to dopant spectroscopy in other quantum solids/fluids, such as solid hydrogen or helium nanodroplets. S. Kanorsky and one of us (AW) have pioneered and developed the original field of sHeMIS research at the Max-Planck-Institute for Quantum Optics in Garching (Germany) more than a decade ago. The studies were later continued and extended at the Institute for Applied Physics of the University of Bonn and are being pursued by our team since 2000 at the Physics Department of the University of Fribourg (Switzerland).

Helium solidifies only under pressure. This is the main obstacle for the preparation of doped helium crystals and the primary reason why it has taken many decades to extend standard MIS methods to helium

matrices. In conventional MIS, the doped samples are prepared by condensing the host and the guest (dopant) substances on a cold finger, with the dopant coming from a thermal jet, a discharge plasma, or a laser ablation target. With solid helium one has first to prepare the host solid and then dope it with the guest substance using a procedure described herein.

In this invited paper we review our research on defect structures formed by atoms and molecules in solid ^{4}He matrices. Optical, radio frequency (rf), and microwave resonance spectroscopy was used to study the samples with and without external magnetic and electric fields. It will not pass unnoticed that this review has a strong focus on our own activities in the field. This simply reflects the fact that, aside from a single publication, there has been, to our knowledge, no other report on optical experiments performed on atomic/molecular defect structures in solid helium.

In this review we will not cover a related field of research originally developed by a group in Chernogolovka, who studies so-called impurity–helium solids formed by condensing a jet of impurity–helium gas mixture into liquid helium [3]. In those studies a highly porous structure composed of frozen impurity (H_2, D_2, N_2, Ne, Kr) clusters is formed inside of bulk *liquid* helium. X-ray scattering, ultrasound propagation, and magnetic resonance (ESR) studies of such samples have been reported. A review of some recent achievements in this field can be found in [4]. Recently the doping technique was modified and first results on doped *solid* helium were reported [5,6].

Among all the known cryocrystals solid helium plays an outstanding role due to its macroscopic quantum nature. This quantum aspect of solid helium also plays a prominent role in the studies described below. The softness of solid He, and, to a lesser extent that of solid hydrogen, is due to the large amplitude zero-point fluctuations of the constituents which allows any entrapped or implanted species, hereafter called defects or dopants, to conserve their symmetry to a large extent. As a rule the spectra of the defects have a simpler structure than the one encountered for defects held in the more rigid conventional matrices. Moreover, the defect can impose its own symmetry on the local environment of the trapping site. Solid helium has the further advantage that it has a symmetric and a uniaxial crystalline phase (at low pressures) between which one can easily switch by changing the temperature or the pressure of the matrix. A comparison of the dopants' properties in both phases has allowed the detailed study of small changes in the trapping-sites symmetry when the phase boundary is crossed.

The paper is organized as follows. In Sec. 2 we will review the main properties of solid helium which are relevant for the experiments, and in Sec. 3 we describe the structure of the atomic defects in solid helium and introduce the so-called atomic bubble model, originally developed for trapped electrons, but which has been successfully extended for the description of optical properties of the trapped species. The next four sections are devoted to experimental studies. In Sec. 4 we describe the details of the various experimental apparatus used for the different studies and in Sec. 5 we present the results of the purely optical studies of atoms, exciplexes and the recently-observed diatomic molecules. In Sec. 6 we introduce the optically detected magnetic resonance (ODMR) technique, a powerful method for studying spin physics in dilute samples of paramagnetic atoms, which combines magnetic resonance with optical preparation and detection. ODMR has been the center of our activities for many years and we will cover the topics of optical pumping, relaxation times, hyperfine transitions, and Stark interactions. Section 7 finally discusses the effects of small bubble deformations on the optical, microwave, and rf spectra. The paper ends with remarks regarding the use of He isolated atoms to search for a permanent electric dipole moment of the electron (Sec. 8) and with a concluding Section 9.

2. Solid ^{4}He

Helium, either ^{3}He or ^{4}He, has the unique property of being the only natural substance which stays liquid under its vapor pressure down to the absolute zero of temperature. Details of the p–T phase diagram of ^{4}He are shown in Fig. 1 from which it can be seen that the solid phase can only be reached by applying pressure p in excess of 25 bar. Under that condition,

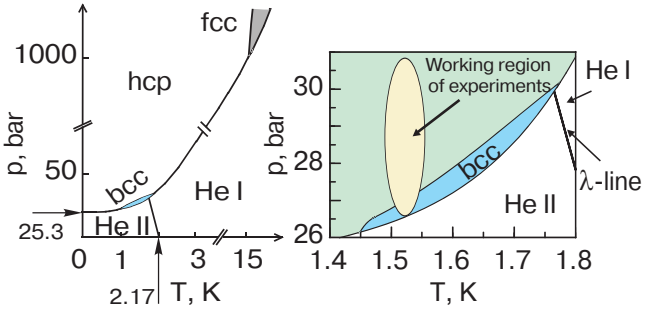

Fig. 1. ^{4}He phase diagram. He I and He II denote the normal fluid and the superfluid phase, respectively. The solid phases are labeled according to their crystalline structures: bcc (body-centered cubic), hcp (hexagonally close-packed), and fcc (face-centered cubic). The p–T region studied in our experiments is shown on the right panel.

^{4}He crystallizes into three different crystalline structures depending on T and p [7]. The (isotropic) body-centered cubic (bcc) and the (uniaxial) hexagonally close-packed (hcp) structures can be obtained at moderate pressures. Above 1000 bar and 15 K, ^{4}He solidifies in a face-centered cubic (fcc) structure as do all the heavier rare gases.

The exceptional behavior of He can be understood as a manifestation of macroscopic quantum properties. The interaction between neighboring He atoms at small internuclear separations is dominated by the Pauli repulsion between their closed electronic S-shells. At intermediate distances, an attractive induced dipole–dipole interaction dominates, however, due to the small electric polarizability, $\alpha = 3.33 \cdot 10^{-4}$ Hz/(V/cm)^2 the attraction is very weak and cannot produce a bound state. Even at $T = 0$, due to the Heisenberg uncertainty principle $\Delta x \Delta p \sim \hbar$, the localization of a helium atom requires a zero-point kinetic energy $E_0 = \Delta p^2/2M$ which is much larger than the potential well depth. As a consequence helium stays liquid at any temperature and the solid phase can be produced only under high pressure which forces the localization of the helium atoms. Due to their very low mass, He atoms have a large thermal de Broglie wavelength ($\lambda_{DB} \approx 7$ Å at $T = 1.6$ K) and are thus strongly delocalized. When the solid is created under pressure the atomic wave functions exhibit a large mutual overlap giving the crystal a macroscopic quantum nature. The substances whose zero-point energy E_0 is comparable to their potential energy U are called quantum solids (liquids) and are characterized by the parameter $\Lambda = E_0/U$ [7]. The value of Λ for solid He is larger than 1, while for all other solid rare gases it is smaller than 1.

Quantum solids are very soft and extremely compressible. These properties distinguish helium crystals from all other rare gas matrices and play an important role in the formation of the so-called *atomic bubbles* which are so central to the research reported below.

3. The atomic bubble model

The structure of the trapping site of an alkali atom in liquid or solid He is described by the so-called bubble model. In this model helium is treated as a continuous medium characterized by its elastic properties. This is justified by the quantum nature of the matrix, i.e., the strong overlap of the helium atoms wave functions arising from the zero point oscillations. The interaction between any alkali impurity atom and the surrounding He is strongly repulsive due to the Pauli repulsion between the valence electron of the atom and the closed S-shell of the He atoms. Because of its quantum nature the helium crystal is very compressible, both by external and by internal pressure. The repulsion of helium by an embedded alkali atom exerts an internal pressure by which helium atoms are expelled from the volume occupied by the valence electron of the alkali. In this way a small cavity is formed which has been called an «atomic bubble». The shape of the bubble reflects that of the trapped atom's electron orbital, and its size is determined by the balance between the impurity–helium repulsion and the external pressure on the bubble surface. The equilibrium configuration can be found by minimizing the total energy of the impurity plus bubble system here modelled via

$$E_{\text{tot}} = \int U(\mathbf{R})\rho(\mathbf{R})\, d^3\mathbf{R} + pV_{\text{bubble}} + \\ + \sigma S_{\text{bubble}} + \frac{\hbar}{8M}\int \frac{(\nabla\rho)^2}{\rho}\, d^3\mathbf{R}\,. \qquad (1)$$

The first term in Eq. (1) represents the interaction between the alkali atom and the He atoms, where $\rho(\mathbf{R})$ describes the He density as a function of the distance $\mathbf{R}$ to the impurity atom. The pair potential $U(\mathbf{R})$ depends on the electronic state of the dopant and has an angular dependence for states with a nonvanishing orbital momentum L. For the sphericaly symmetric ground states of alkali elements, it depends only on $R = |\mathbf{R}|$ and the defect structure can be parameterized using two parameters: the bubble radius and the thickness of the bubble interface. Theoretical pair potentials $U(\mathbf{R})$ for different electronic states of all alkali elements interacting with a He atom in its ground state are given in the literature [8].

The energy of the bubble in condensed helium is composed of the pressure-volume work, pV_{bubble}, the energy from surface tension, σS_{bubble}, and the volume kinetic energy, i.e., the excess zero-point energy due to the localization of the He atoms at the bubble interface, given by the fourth term of Eq. (1).

For a spherically symmetric defect, the helium density $\rho(R)$ is described by the radial trial function

$$\rho(R, R_b, \alpha) = \\ = \begin{cases} 0\,, & R < R_b \\ \rho_0\{1 - [1 + \alpha(R - R_b)]\exp[-\alpha(R - R_b)]\}, & R > R_b \end{cases} \qquad (2)$$

where ρ_0 is the bulk helium density and the parameters R_b and α are measures of the bubble radius and bubble interface thickness, respectively, and which are adjusted to minimize the total defect energy E_{tot}.

This approach was first introduced by Jortner et al. [9] to model a free electron in liquid He, for which the expression «electron bubble» was coined, and was later extended to atomic impurities in liquid [10,11]

and in solid [12] He. It successfully models optical absorption and emission spectra using the standard adiabatic line-broadening theory [13], in which lineshapes are calculated from the Fourier transform of the optical dipole autocorrelation function $C(\tau)$ represented by

$$C(\tau) = \exp\left\{-\int [1 - \exp(-i\Delta\nu(R)\tau)]\rho(R)\, d^3R\right\}, \quad (3)$$

where $\Delta\nu(R)$ is the shift of the dopant's transition energy due to a single He atom located at position R. According to the Franck–Condon principle, the absorption (emission) line shape may then be calculated assuming a bubble configuration corresponding to the ground (excited) state.

4. Experimental setup

All our experiments reported in this paper were performed using the same basic cryogenic setup, one which allows us to create a He crystal, to dope it with alkali (Cs, Rb) atoms and molecules, and to perform spectroscopic studies in the optical, microwave, or in the radio frequency domain, either with or without static magnetic and electric fields. In this section we will first describe the cryostat and the doping procedure, and then present details of the experimental arrangements for the different studies.

4.1. Sample preparation

The He crystal is grown in a cubic (inner dimensions 6×6×6 cm, wall thickness 1.7 cm) pressure cell made of copper. The cell has five optical windows, one on each side and one on the top of the cell. It is immersed in a liquid helium bath contained in a specially designed cryostat with optical windows that are coaxial with the cell windows (Fig. 2). Before the experiment, the cryostat is filled with 80 liters of liquid He

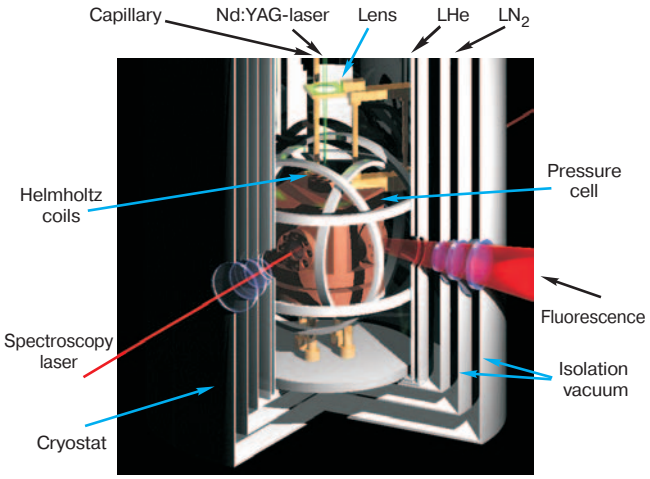

Fig. 2. Vertical cut trough the cryostat, showing the pressure cell and the triaxial system of Helmholtz coils inside the helium bath.

at 4.2 K and then cooled to 1.5 K by pumping on the liquid He. The holding time of the cryostat depends on the heat load (absorption of laser radiation, high voltage leakage currents, heat conduction via electrical connections to the cell volume, etc.). It typically allows us to perform continuous measurements during 2–4 days. After filling the bath, helium gas is admitted into the pressure cell via a liquid nitrogen cold trap to remove condensable gases. This transfer goes via a thin (2 mm diameter) capillary that minimizes heat exchange. The helium used to form the matrix comes from a 200 bar storage bottle (purity 99.9999%) connected to the capillary via a buffer volume, which allows the control of the helium pressure in the cell by a needle valve. The temperature is measured by two germanium resistors located in the pressure cell and in the He bath, respectively.

After reaching the working temperature of 1.5 K, a He crystal is produced by increasing the pressure in the cell to a value above the solidification pressure (26.4 bar), typically to about 29.5 bar.

Implantation of alkali atoms in the He crystal is performed by laser ablation from the target (cut glass ampule containing 0.5 g of the metal under investigation) installed under an inert gas atmosphere at the bottom of the pressure cell in the preparation process. The successive stages of the implantation process are shown schematically in the lower panels of Fig. 3. The top row of the same figure shows photographs taken through the side-windows of the cryostat and pressure cell during the implantation. First, the beam of a frequency doubled Nd:YAG laser (λ = 532 nm, pulse energy 20 mJ, repetition rate 1 Hz) is focused, by a lens mounted just above the top window of the pressure cell, onto the alkali metal target. The heat deposited into the sample by each pulse melts a portion of the crystal just above the target (Fig. 3,*a*). Simultaneously with the melting of the crystal, individual atoms, molecules, and clusters are ejected from the target and are distributed throughout the molten helium region by convection (Fig. 3,*b*). By moving the lens upwards during this phase we displace the focal point and hence — the position of the molten part in the crystal until the column of liquefied helium has risen to the upper end of the window. After the desired column height is reached, the Nd:YAG laser is switched off and the molten He resolidifies, thereby trapping the implanted species in the previously molten column-like region (Fig. 3,*c*). This doping procedure was initially reported [14] for Ba and Cs and was later applied in all our studies including those with Rb and Rb/Cs mixtures. The implanted species are trapped in the solid matrix and do not escape from the trapping volume for many hours. This represents the main

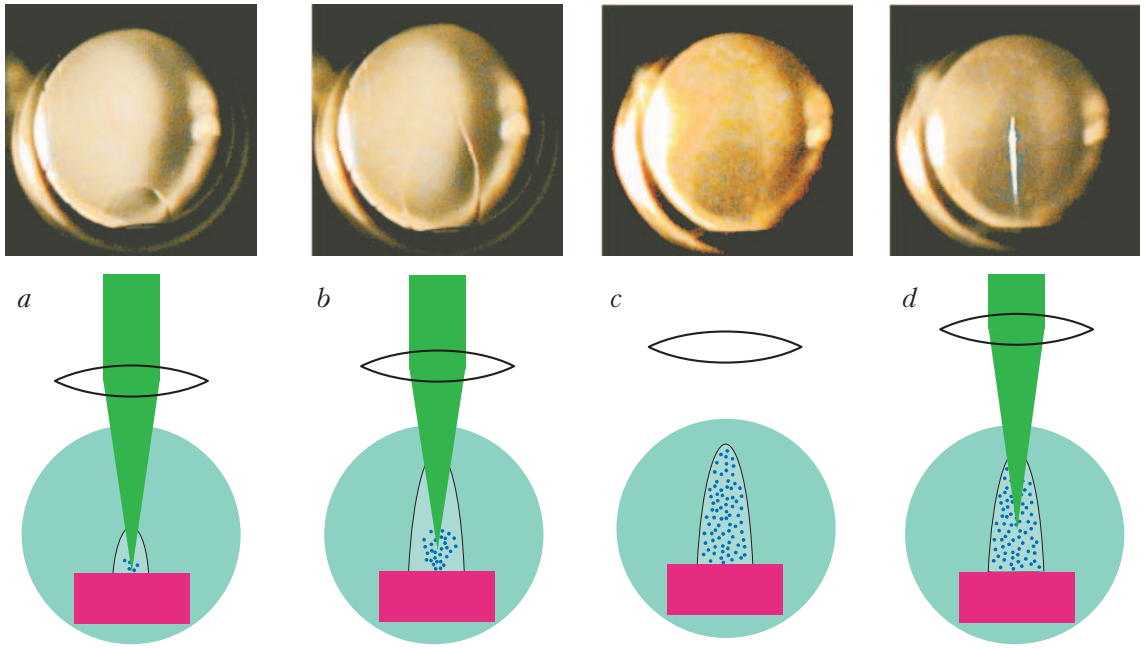

Fig. 3. Different steps of the implantation process shown schematically (lower panels) and as frames of a video recording taken through one of the lateral window of the cryostat and the pressure cell (upper row). In (*d*) a frame was selected in which fluorescence induced by the Nd:YAG laser can be seen. Details are given in the text.

advantage of using solid He as compared to liquid He, where the implanted atoms are quickly washed out of the observation volume by convection.

Depending on implantation conditions (He pressure, laser pulse energy, repetition rate and the total number of pulses) the doped part of the crystal has either a greyish or bluish color. The color is due to strong absorption and scattering of light by metallic clusters produced by the ablation. The peak of the optical absorption spectrum of this background is in the near infrared (for Cs) or in the red (for Rb) part of the spectrum, and depends on the cluster size distribution. The comparison of measured extinction spectra with calculations based on the Mie theory of light scattering by small particles [15] reveals a typical cluster size on the order of 50 nm and a number density of about 10^{10} cm^{-3}, comparable to or even larger than the density of isolated atoms (typically about 10^9 cm^{-3}).

The signal of interest for our spectroscopic studies is produced either by atoms or by molecules trapped in the crystal. Because of the softness of the He crystal and of the large number of defects due to the brute force preparation process, the implanted atoms do diffuse within the doped region. When an atom comes near another atom or cluster, it will be attracted by van der Waals forces to form a molecule or a larger cluster, thereby reducing the number of atoms available for the experiments. The number of atoms can be increased again by destroying the clusters and molecules by applying pulses from the same Nd:YAG laser, focused in the center of the doped region (Fig. 3,*d*) with a reduced pulse energy and a lower repetition rate than used in the implantation process (to avoid melting of the crystal).

4.2. Setup for optical spectroscopy

A top view of the typical setup for purely optical studies is shown in Fig. 4. The dopants in the helium crystal are excited by radiation from an optical parametric oscillator (OPO) pumped by the third harmonic (λ = 355 nm) of a pulsed Nd:YAG laser. The tuning range of the OPO covers the large spectral intervals of 780–2400 nm (idler beam) and 450–700 nm (signal beam). The repetition rate of the laser pulses is

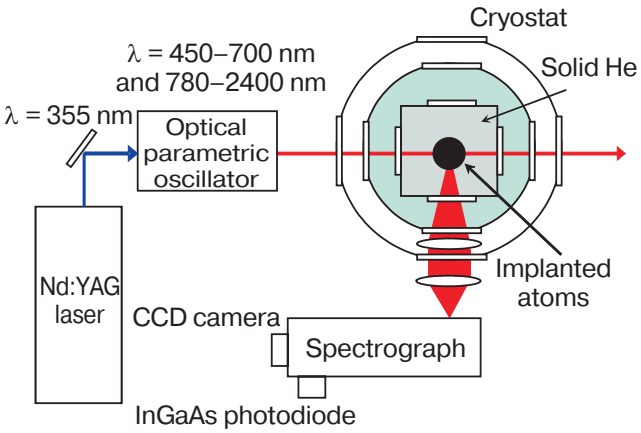

Fig. 4. Horizontal cross section of the cryostat and the pressure cell (not to scale) and top view of the optical spectroscopic setup.

10 Hz and the average light power is controlled by means of a $\lambda/2$ plate and a polarizer. During the experiments, the OPO power is kept at a level of 1 mW to prevent melting of the He crystal. For spectroscopy in the range between 720 and 780 nm, which cannot be accessed by the OPO, we use a tunable cw Ti:Sa laser pumped by a frequency doubled Nd:YVO_3 laser.

The laser induced fluorescence from the sample volume (≈ 3 mm^3) is collimated by a lens in the cryostat and focused into a grating spectrograph which has a resolution of 0.2 nm. To access different parts of the spectral domain, two different photodetectors are mounted to the spectrometer. Visible and near-infrared fluorescence is detected by means of a CCD camera which allows the recording of complete spectra, while for wavelengths above 1 μm an InGaAs photodiode is used. In the latter case the grating is rotated by a stepper motor, and the spectra are recorded point by point.

This setup was used in our studies of laser-induced fluorescence of atomic Cs, Cs*He_N exciplexes [16,17], atomic Rb, Rb*He_N exciplexes [18], and Rb_2 molecules [19].

4.3. Magnetic resonance spectroscopy

Optically detected magnetic resonance spectroscopy relies on driving magnetic dipole transitions between split Zeeman levels in combination with optical preparation and detection and will be discussed in detail in Sec. 6. Some of the main elements of the corresponding experimental setup are shown in Fig. 2. The static magnetic field is produced by three pairs of superconducting Helmholtz coils mounted orthogonally to each other around the pressure cell, inside the He bath. A highly stable field is produced by the coils operated in a self-sustained (persistent) current mode [20]. The recording of ultra-narrow magnetic resonance lines requires special care in the choice of low-temperature (and in some cases high-voltage) compatible nonmagnetic components and in the design of the pressure cell. For example, indium — the most convenient material for vacuum/pressure seals at low temperatures becomes superconductive and may maintain a permanent electric current, whose magnetic field will perturb the measurements. In order to avoid this problem, all sealings in the pressure cell are made of pure aluminum. Laboratory fields and gradients are suppressed by a cylindrical three-layer magnetic shield surrounding the whole cryostat.

The sample is irradiated by a circularly polarized cw laser beam resonant with the D_1 transition of the implanted atoms. For Cs a near infrared diode laser (1 mW) is used, whereas for Rb we use 1 mW of radiation from the Ti:Sa laser. Laser-induced fluorescence from the implanted atoms is collected in the same way as in the optical spectroscopic experiments and detected either by a photomultiplier or an avalanche photodiode. In these experiments we do not use the spectrograph but rather an interference filter to suppress the scattered laser light. As discussed in Sec. 5, the fluorescence of Rb atoms in solid He is so weak that it escaped observation for a long time. For this reason the magnetic resonances in Rb were detected by monitoring the transmitted intensity of the pumping laser.

The magnetic transitions are induced by an oscillating magnetic field produced by a second system of Helmholtz coils mounted inside the pressure cell (shown in Fig. 5, not visible in Fig. 2). The current to these coils is supplied by a waveform generator through an electric feedthrough at the bottom of the

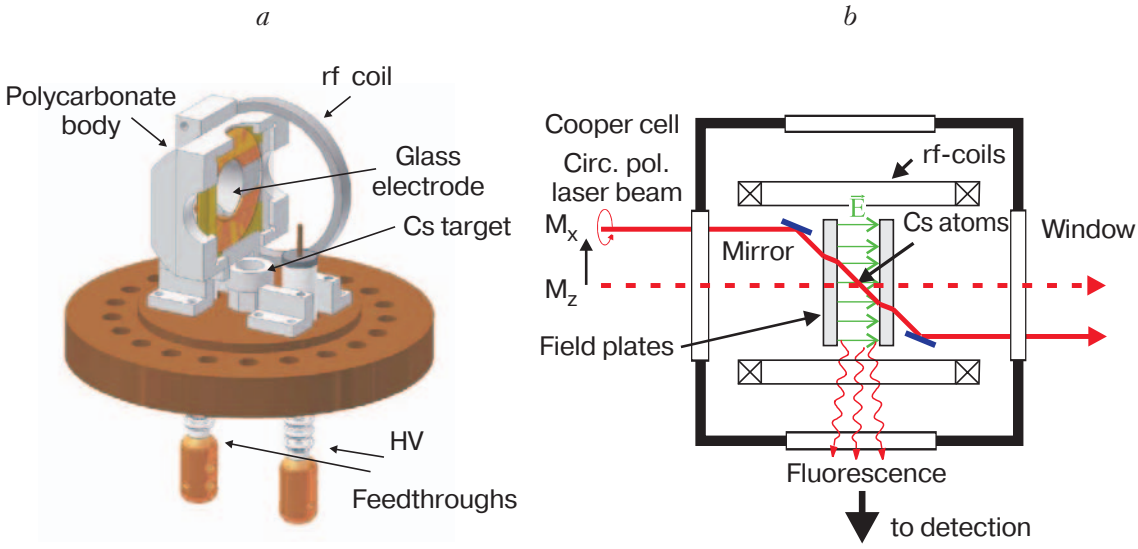

Fig. 5. (*a*) the bottom flange of the pressure cell of Fig. 2 with one of the rf-coils and one of the HV electrodes shown; (*b*) top view of the set-up for magnetic resonance experiments with electric fields.

cell. The ODMR technique was also used to study the microwave transition between the two hyperfine levels of the ground state of Cs in solid He (ν = 9.2 GHz). In that case, the oscillating magnetic field was produced by a microwave frequency synthesizer and irradiated through one of the fused silica optical windows of the pressure cell.

A separate subsection of this paper is devoted to our very recent studies of the Stark effect on the magnetic resonance transitions in Cs. For that study, the ODMR setup described above was modified in order to apply a large static electric field to the Cs-doped He crystal. A bipolar high voltage produced by two identical power supplies of opposite polarity was delivered to the sample via HV cables traversing the top flange of the cryostat, then the helium bath, inside of which they were connected to specially designed feedthroughs mounted on the bottom of the pressure cell (Fig. 5). The feedthroughs are connected to a pair of electrodes (spacing 6.0 mm), cut from float glass and coated on one side with a transparent conductive layer of tin oxide. Pure liquid and solid He are excellent electric insulators. In practice, the magnitude of the applied electric field strength is limited by the leakage current through the doped He crystal. Increasing the field strength above 50 kV/cm results in the melting of the sample and produces an electric breakdown in the cell.

5. Optical spectroscopy

5.1. Atomic fluorescence

First systematic spectroscopic studies of atoms in solid He were carried out in experiments with Ba, for which a good agreement with the predictions of the bubble model was obtained [10,12,21]. Later those studies were extended to alkali elements. Here we discuss the absorption and fluorescence of cesium atoms in solid He studied in great detail in [12,17,20]. Cesium is the only alkali element which emits a strong atomic fluorescence in a *solid* He environment. The light alkalis Li, Na, and K do not emit any fluorescence neither in solid nor in liquid He. Rb represents an intermediate case, as it emits fluorescence in liquid He, but its fluorescence is strongly quenched with increased He pressure [22]. Only recently, a very faint fluorescence of atomic Rb was observed in solid (hcp) He following excitation of the D_1 and D_2 transitions [18]. The quenching of the atomic fluorescence is due to the formation of molecular complexes by excited nP states of alkali atoms and the surrounding helium atoms, so-called exciplexes [12,23]. As discussed in Sec. 5.2, the formation of the exciplex becomes possible when the alkali–helium interaction is stronger than the spin–orbit coupling in the alkali atom. Therefore the probability of the exciplex formation is much larger for lighter alkalis, in which the spin–orbit coupling is weak, and it increases with the density of He, i.e., with rising He pressure, or when going from liquid to solid phase.

Typical fluorescence spectra of Cs in solid He are shown in Fig. 6,*a* for the bcc and hcp crystalline phases. Only fluorescence on the D_1 transition can be observed, as atoms excited to the $6P_{3/2}$ state are quenched by the interaction with the matrix to form either atoms in the excited $6P_{1/2}$ state or to form Cs^*He_N exciplexes. An absorption spectrum recorded by scanning the excitation laser and monitoring the intensity of the D_1 fluorescence, is shown in Fig. 6,*b*, where both the D_1 and the D_2 absorption lines are detected. The position of the D_1 line center measured in

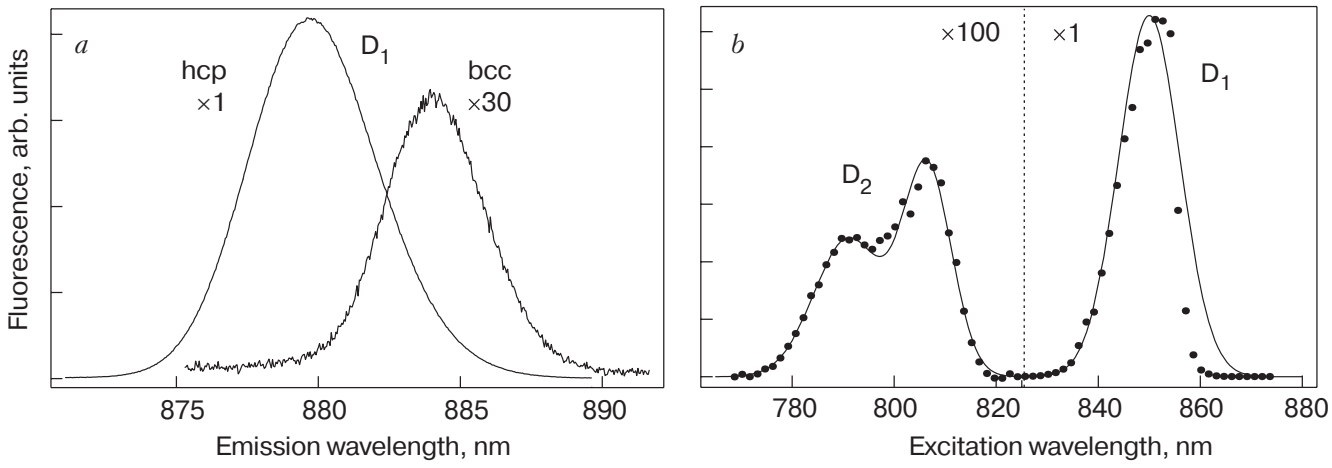

Fig. 6. Experimental emission spectrum of the D_1 line of Cs following D_1 excitation in the bcc and hcp phases of solid ^{4}He (*a*) and excitation spectrum of the D_1 and D_2 transitions detected via fluorescence on the D_1 line of Cs in hcp (*b*). The resonance wavelengths of the same transitions in the free Cs atom are 894 and 852 nm, respectively.

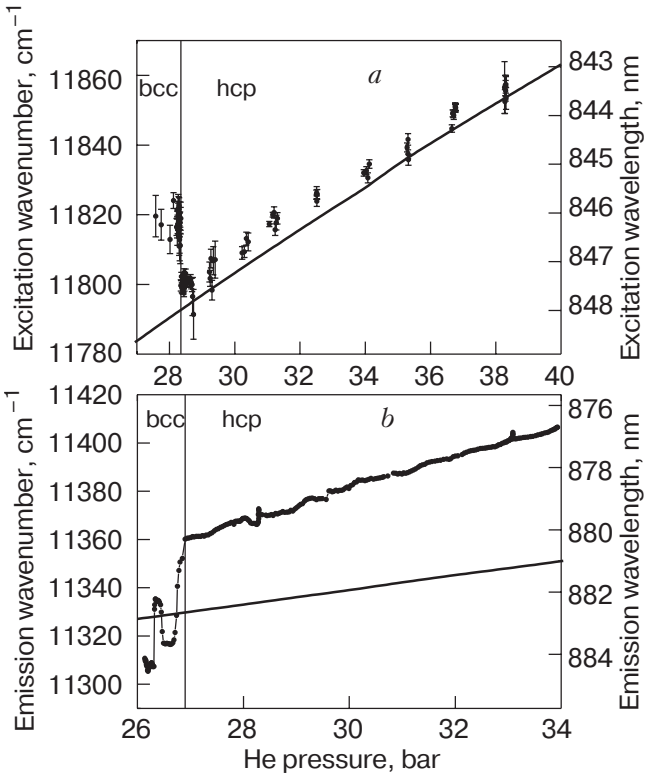

Fig. 7. Dependence of the D_1 absorption (*a*) and emission (*b*) lines of Cs in solid He on He pressure. The experimental data are shown as dots and the straight lines are resonance positions calculated [20] using the spherical bubble model. The D_1 transition in the free Cs atom is at 894 nm (11186 cm^{-1}).

absorption and emission is plotted in Fig. 7 as a function of He pressure.

As one can see in Figs. 6 and 7, both the absorption and the emission lines in solid He are strongly broadened and blueshifted with respect to the free Cs atom. The shift and the broadening are more pronounced in the absorption spectra than in the emission spectra. Very similar spectra were obtained in a pressurized liquid He environment, where a quantitative agreement with the predictions of the bubble model was demonstrated [11]. The blueshift of the spectral lines can be understood from the changes of the bubble size that occur during an optical absorption–emission cycle (Fig. 8). The blueshift is due to the fact that the electronic density distribution of the excited 6*P* state of Cs is spread over a larger volume than that of the ground state. The interaction with the bubble shifts both levels towards higher energies, but the excited state, due to its larger interaction energy, shifts more than the ground state and hence the transition wavelength shifts to the blue. The absorption takes place in a smaller bubble, whose size is determined by the Cs ground state and the blue shift is particularly large.

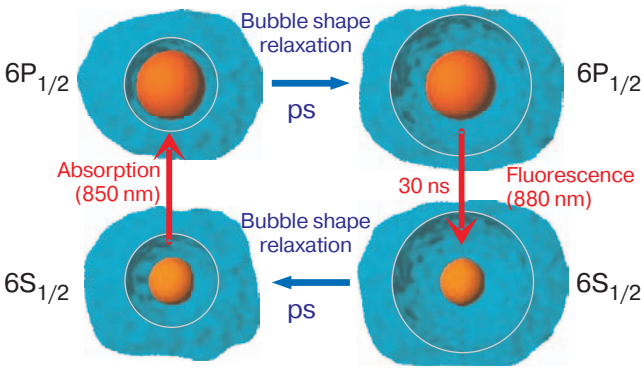

Fig. 8. Expansion and shrinking of the atomic bubble during an optical absorption–emission cycle.

After the excitation of the impurity atom, the bubble expands and a new equilibrium configuration minimizing the total energy is realized on a time scale much shorter than the radiative lifetime of the $6P_{1/2}$ state. The emission then occurs in a larger bubble that reflects the size of the excited state and therefore the broadening and the shift of the emission lines are smaller.

The bubble model also explains the observed increase of the spectral width and the rate at which the lines shift with He pressure, as shown in Fig. 7, however the abrupt changes of the absorption/emission wavelengths at the liquid–bcc and bcc–hcp phase transitions have not yet been explained quantitatively (see Sec. 7).

The only atoms of which optical absorption and emission spectra in solid helium were studied are ^{85}Rb, ^{87}Rb, ^{133}Cs, ^{137}Ba, and ^{169}Tm. While the (optical) valence electron of alkali atoms interacts with the helium matrix with an energy comparable to the spin–orbit interaction, the optical electron of the lanthanide thulium behaves quite differently. Its optical transition occurs between two unfilled shells (4*f* and 5*d*) which are shielded from the matrix by outer electrons which do not participate in the optical transition. Ishikawa et al. [24] have measured absorption and emission lines from Tm in superfluid and solid helium as well as excited state lifetimes. Because of the shielding from matrix effects the authors of [24] could observe widths of optical resonance lines on the order of 0.1 nm (limited by the resolution of the spectrometer). To our knowledge this is the only experiment besides our own which has reported an optical study of atoms in solid helium. We also mention here the related optical spectroscopic studies of electron bubbles in solid He, pioneered by Mezhov-Deglin and Golov [25–27].

5.2. Alkali—helium exciplexes

The term «exciplex» stands for excited state complex and refers to molecular complexes which form bound or quasibound states only when one of their constituents is in an excited state. Exciplexes composed of an alkali atom in the *nP* state and one or several ground state He atoms were considered for the first time in [12,23] to explain the quenching of the laser-induced fluorescence from light alkalis in liquid and solid helium. A first experimental confirmation of that proposal was obtained by a group in Kyoto in a series of experiments that covered all alkali elements in liquid He and cold He gas [28–30]. Such complexes were also observed and extensively studied in experiments with alkali doped superfluid helium nanodroplets [31–36]. We also mention related experimental studies of Ag^*He_2 [37] and Mg^*He_N [38,39] exciplexes in liquid He and that of $Ba^{+*}He$ [40] in cold He gas. In solid helium, the formation of Cs^*He_N exciplexes was reported by our group for the first time in [16] and described with more experimental and theoretical details in [17,41]. More recently we have extended these studies to Rb^*He_N in solid He [18].

The exciplexes are typically detected via their laser-induced fluorescence which can be excited at the wavelengths of the resonant atomic transitions. The characteristic feature of exciplex emission, and the reason why it has escaped observation for many years, is its strong red shift with respect to the corresponding absorption lines. For instance the Cs^*He_N can be formed after excitation at 800 nm, while it fluoresces at 1400 nm. Typical spectra of Cs^*He_N and Rb^*He_N in the hcp phase of solid He excited at the D_2 atomic transitions of Cs and Rb, respectively are shown in Figs. 9,*a* and 9,*b*.

The theoretical model for describing the optical properties of exciplexes developed in [17,41] is based on adiabatic alkali—helium pair potentials [8], which are strongly anisotropic for the *nP* states of the alkalis. The alkali—helium interaction at intermediate interatomic distances is dominated by the Pauli repulsion between their valence electrons. When a He atom approaches from a direction along which the electronic density of the alkali orbital is high, it experiences a strong repulsion. However, the *nP* orbitals possess nodal planes, or nodal axes, along which the electronic density is zero so that the helium atom can come close enough to experience a van der Waals attraction by the alkali's core. In this case a short lived weakly bound or quasibound complex can be formed. For the light alkalis, in which the spin—orbit interaction is much weaker than the interaction between the impurity and the He atoms, the excited state orbital is well

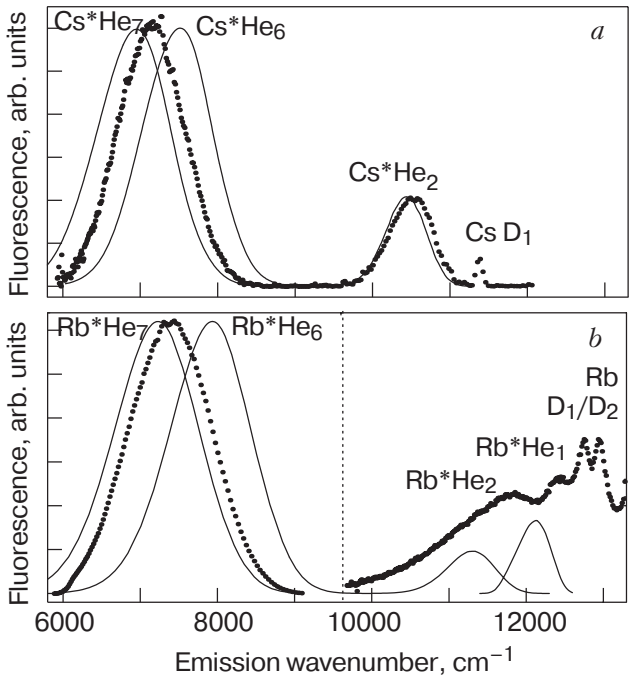

Fig. 9. Experimental emission spectra of Cs^*He_N (*a*) and Rb^*He_N (*b*) exciplexes in hcp solid He excited at the D_2 transitions of Cs and Rb, respectively. The atomic D_1 emission line of Cs and the D_1/D_2 doublet of Rb are visible on the blue side of the exciplex spectra. The vertical dotted line in (*b*) separates two spectral regions with different vertical scales. The emission of atomic Rb and $Rb^*He_{1,2}$ exciplexes on the right part of the figure is several orders of magnitude weaker than any other spectral feature.

represented by a dumbbell-shaped P_z orbital which allows several He atoms to be bound around its waist. For the heavier alkalis, Rb, and in particular for Cs, the spin—orbit interaction which generates the fine-structure splitting of the *nP* state into $nP_{1/2}$ and $nP_{3/2}$ states becomes comparable to the impurity—helium interaction and the symmetry of the state is given by its total angular momentum J.

The $nP_{1/2}$ state is spherically symmetric and hence repulsive for He. The $nP_{3/2}$ state, on the other hand, has two distinct orbitals depending on the projection $|M_J|$ of J on the internuclear axis. The approaching He atom sees either a repulsive dumbbell-shaped orbital in the $M_J = \pm 1/2$ configuration oriented along the direction of the approach, or an attractive apple-shaped orbital ($M_J = \pm 3/2$ configuration) with two dimples on opposite sides, again along the direction of approach [23].

In agreement with the discussion above, we observed the diatomic and triatomic exciplexes $Cs(6P_{3/2})He_2$, $Rb(5P_{3/2})He_1$, and $Rb(5P_{3/2})He_2$, whose emission lines at 10500, 12400, and 11800 cm^{-1}, respectively, are shown in Fig. 9. However, the two strongest and most redshifted emission bands originate

from different complexes. Due to the (spin–orbit uncoupling) mixing of the two fine-structure components by the alkali–helium interaction the $nP_{1/2}$ state acquires the character of the $nP_{3/2}$ state and its orbital becomes dumbbell-shaped. This mixed state allows several He atoms to be bound around its waist, as in the case of the lighter alkalis. These complexes fluoresce at 7200 cm^{-1} (Cs^*He_N) and 7400 cm^{-1} (Rb^*He_N).

The model presented in [17,18,41] has allowed us to calculate the emission spectra of the exciplexes as well as their vibrational and total energies. However, the interaction of the exciplex with the surrounding He bulk has so far not been taken into account. Based on the model, the number of bound He atoms can be estimated to be $N = 6$ or 7 (see Fig. 9). Alternative theoretical studies of Cs^*He_N [42], Rb^*He_N [29], and the closely related K^*He_N [43] suggest $N = 6$ as the most probable number of bound He atoms.

Owing to the very high He density and the compact bubble structure in solid helium, sHeMIS has proven, in comparison to other experimental techniques (helium nanodroplets, cold helium gas), to be particularly well suited for the formation and investigation of exciplexes with a maximally allowed number of bound He atoms. Due to the large rate of collisions with surrounding helium atoms, the attachment of He atoms in solid He proceeds at a much faster rate than in any other environment and stops only when all vacancies are occupied, i.e., by the filling of the two dimples of the $nP_{3/2}$ orbital or of the ring-shaped belt around the waist of the perturbed $nP_{1/2}$ orbital. All intermediate complexes occur only as transients which have no time to fluoresce and who thus do not contribute to the emission spectrum. A very similar behavior was observed in liquid He [28–30], with the difference that in that case the perturbation of the $6P_{1/2}$ state of Cs was not strong enough to allow the formation of the ring-shaped complex. The largest complex seen in superfluid helium is the triatomic $Cs(6P_{3/2})He_2$ exciplex [28].

5.3. Alkali dimers

Absorption and emission spectra of alkali molecules (dimers) were extensively studied in experiments with alkali-doped helium nanodroplets [36,44–49], where all homonuclear and some heteronuclear dimers were formed and investigated. However, until recently, there had only been very few investigations of alkali dimers in bulk condensed helium. In superfluid He only some (unassigned) bands of Na_2 and Li_2 have been reported [50].

In our recent experiments [19] we observed for the first time alkali molecules in solid He. In those experiments we studied the fluorescence spectrum of Rb-doped solid He under laser-excitation in the broad spectral range from 450 to 1000 nm and found a remarkable result. Besides atomic and exciplex emission, a single additional spectral feature was observed at 1042 nm (Fig. 10,*a*). We have assigned this emission band to the forbidden $X^1\Sigma_g \leftarrow (1)^3\Pi_u$ transition of Rb_2. We base this assignment on the spectral structure of the free dimer and on the observation of a long lifetime of the fluorescing state which points to its metastable character (Fig. 10,*b*). Our most striking observation is the fact that this (single) emission band can be excited on 9 distinct absorption bands of Rb_2 in the range of 450 to 900 nm (Fig. 11), including transitions originating from the $X^1\Sigma_g$ ground state and from the lowest triplet state $(1)^3\Sigma_u$. The measured and calculated spectral positions of these bands are given in Table 1. The calculation of

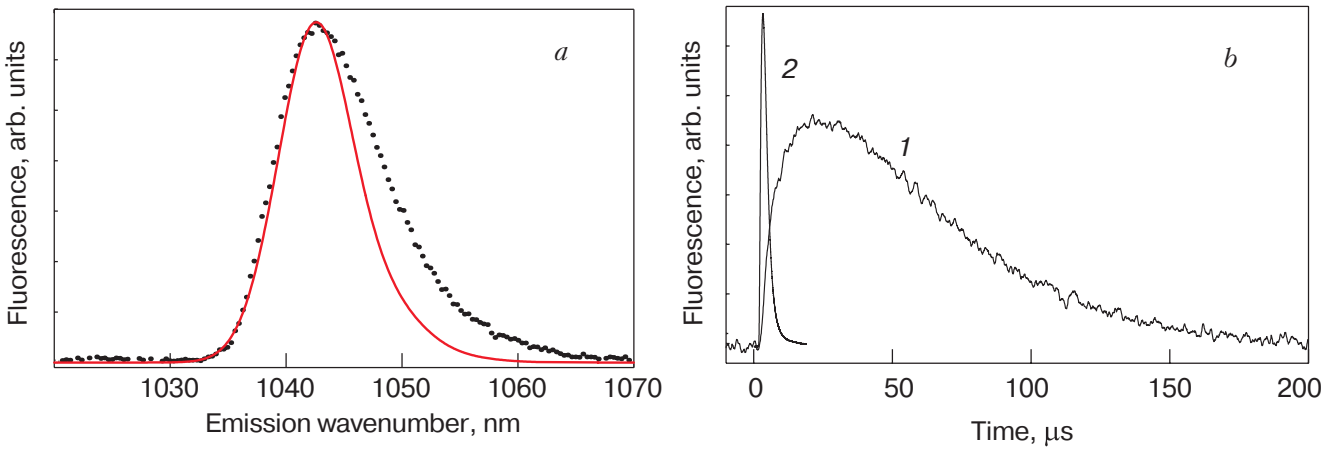

Fig. 10. (*a*) Experimental (points) and calculated (solid curve) emission spectra of $(1)^3\Pi_u \rightarrow X^1\Sigma_g$ transition in Rb_2. The theoretical curve was obtained by shifting the calculated spectrum by 20 nm to the red. (*b*) Measured pulse shapes of the molecular fluorescence at 1042 nm (curve *1*) and scattering of the excitation laser light at 842 nm (curve *2*), which represents the time resolution of the photodetector as the actual width of the laser pulse (5 ns) is not resolved.

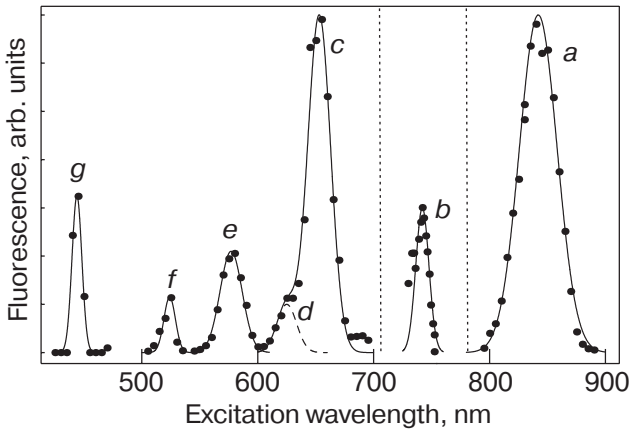

Fig. 11. Measured excitation spectrum of the Rb_2 fluorescence at 1042 nm. Experimental data are shown as points, and the solid lines are fitted Gaussians. The assignment of all peaks is given in Table 1. The dotted vertical lines mark the spectral regions covered by the three excitation sources described in the text. The vertical scales differ for the different intervals. Note that the excitation at the bands *b*, *d*, and *e* also branches to photodissociation channels.

the theoretical band positions assumes that only the lowest vibrational state of the emitting electronic level is populated, but does not take the interaction with the He matrix into account. We attribute the (small) discrepancies between the calculated and measured band positions to this fact.

Table 1. Calculated and measured wavelengths of Rb_2 absorption bands (in nm) in solid He. The labels refer to the corresponding peaks in Fig. 11.

Band	Label	λ_{theor}	λ_{exper}
$X^1\Sigma_g \to A^1\Sigma_u$	*a*	878	842
$(1)^3\Sigma_u \to (1)^3\Pi_g$	*b*	735	742
$X^1\Sigma_g \to B^1\Pi_u$	*c*	664	653
$(1)^3\Sigma_u \to (3)^1\Sigma_g$	*d*	623	622
$(1)^3\Sigma_u \to (2)^3\Sigma_g$	*e*	590	580
$(1)^3\Sigma_u \to (2)^3\Pi_g$	*e*	586	580
$(1)^3\Sigma_u \to (3)^3\Sigma_g$	*f*	507	524
$X^1\Sigma_g \to (2)^1\Sigma_u$	*g*	477	445
$X^1\Sigma_g \to (2)^1\Pi_u$	*g*	464	445

We have also studied the time dependence of this fluorescence in an experiment using pulsed excitation and found a width of the fluorescence pulse of 60 μs (Fig. 10,*b*), much longer than the characteristic lifetime of any allowed electronic transition. The fluorescence pulse has finite rise and decay times, which point to the formation of a state that does not exist in the free dimer. We assign [19] this behavior to the formation of a molecular exciplex state, from which the observed fluorescence emanates.

The experimental observations show that in solid He, due to the interaction with the matrix, all laser-excited molecular states are quenched. The quenching results in the population of the metastable $(1)^3\Pi_u$ state which is the lowest excited state of this molecule. The perturbation of the molecule by the surrounding helium partly lifts the selection rule that forbids the radiative transition from that (triplet) state to the singlet ground state so that the transition $X^1\Sigma_g \leftarrow (1)^3\Pi_u$ can be observed.

We have also observed photodissociation of the Rb_2 molecule into two Rb atoms, one in the ground state and the other in the excited $5P_{1/2}$ or $5P_{3/2}$ state. The latter emits fluorescence at the same wavelength as do individual Rb atoms excited either at D_1, or D_2 transition. The photodissociation spectrum recorded by scanning the excitation wavelength and detecting the atomic fluorescence contains the forbidden molecular bands $(1)^3\Sigma_u \to (2)^3\Sigma_u$ (650 nm) and $X^1\Sigma_g \to (3)^1\Sigma_g$ (490 nm) in addition to the bands *b*, *d*, and *e* shown in Fig. 11 and Table 1.

6. Optical pumping and magnetic resonance

Our initial motivation for entering the field of sHeMIS was the expectation that the helium quantum matrices would be ideally suited for performing high resolution experiments involving spin polarized defects, such as the search for a permanent electric dipole moment of the electron [51]. This expectation was based on two facts: on one hand, ^{4}He has neither an electronic nor a nuclear magnetic moment, so that it has no first order coupling to the spin of the paramagnetic defect. On the other hand, it had been known from the spectroscopy of atoms and ions in superfluid helium as well as from studies of isolated electron bubbles in both liquid and solid helium that the implanted defects locally impose, to a large extent, their own symmetry, i.e., the shape of their electron distribution on the spatial distribution of helium atoms surrounding the defect. Unlike in any other solid state matrix where the symmetry of the dopant is in general lowered due to local field effects, which themselves couple to the dopant's spin via the spin–orbit interaction, one therefore did not expect any coupling (again in lowest order) of the dopant's spin to the local host structure, provided that the dopant had a spherically symmetric electronic wave function, as is the case, e.g., for atomic $S_{1/2}$, $P_{1/2}$, $^1S_0$ states. The spherically symmetric $S_{1/2}$ ground state of alkali metals seemed particularly well suited for testing this hy-

pothesis, and it was expected that a spin polarized sample of such atoms would have an exceptionally long electronic spin relaxation time.

6.1. Optical pumping

The first experimental demonstration of optical pumping of alkali atoms in condensed helium was performed with ^{85}Rb, ^{87}Rb, and ^{133}Cs in superfluid helium [52]. In those experiments, spin polarization was created by optical pumping of rubidium or cesium atoms implanted by laser sputtering into liquid helium.

The efficient process of optical pumping was discovered in the 1950's in vapor phase atomic samples and has since found numerous applications. The resonant scattering of a circularly polarized light beam by the atoms transfers angular momentum from the light to the atoms. In this way the irradiation of the sample with circularly polarized light leads to the creation of spin orientation (dipole polarization) [53] by the redistribution of populations among the ground state Zeeman sublevels. In all optical-pumping sHeMIS experiments carried out to date the optical pumping used excitations to the lowest lying $P_{1/2}$ state, i.e., the so-called $D_1(nS_{1/2} \rightarrow nP_{1/2})$ transition, whose wavelengths (for Cs and Rb) lie in the near infrared. The hyperfine interaction splits the ground and first excited states into two levels with total angular momenta of $F = I \pm 1/2$, where I denotes a nuclear spin. Due to the large homogeneous linewidth of the absorption line in condensed helium (cf. Sec. 5) the hyperfine structure of the transition cannot be resolved, so that the selection rules are those of a $J = 1/2 \rightarrow J = 1/2$ transition. This situation is equivalent to exciting the transition in a vapor or an atomic beam using a spectrally broad light source, as is encountered, e.g., in the optical pumping by resonance radiation from a discharge lamp. One can show that in this case excitation with linearly polarized light does not lead to a redistribution of populations, so that optical pumping can only be achieved with circularly polarized light. It is thus not possible to create an alignment (quadrupole polarization) in the ground state by optical pumping.

After a number of absorption–emission cycles on the D_1 transition nearly all atoms become pumped to the state $|F = I + 1/2, M = F\rangle$ which does not absorb circularly polarized light and which therefore is referred to as «dark state». The polarized sample does not fluoresce and any polarization destroying effect, such as a magnetic resonance transition, leads to a revival of fluorescence. This forms the basis of the optical detection of magnetic resonance.

In 1995 our group showed that efficient optical pumping is also possible with alkali atoms embedded in the cubic phase of solid ^{4}He [54] and, with a reduced efficiency, in the anisotropic hexagonal phase of the matrix [55,56]. In those experiments we demonstrated our original assumption that the spin polarization of alkali atoms in solid helium may indeed be very long lived. In a subsequent study we investigated the optical pumping process in the bcc and in the hcp phase in detail [57]. We found that optical pumping is of the repopulation type, i.e., that the spin polarization created during the optical pumping process in the excited $P_{1/2}$ state, which itself lives for a few 10 ns, is not destroyed by the interaction with the helium matrix. This is surprising at first sight as it is known that this process, whose origin is spin–orbit coupling induced by collisions, occurs in helium gas and becomes more efficient with growing helium pressure. However, in solid helium the collision rate with helium atoms on the bubble interface is so high that the Cs spin has no time to couple efficiently to the short-lived collision induced orbital momentum.

Optical pumping of cesium in the anisotropic hcp phase of helium is much less efficient than in the isotropic bcc phase. We showed that the degree of spin polarization achievable in hcp ^{4}He depends strongly on the value of the magnetic holding field B_0 (see Fig. 19,*b*), while in bcc phase it was found to be independent of B_0 [57]. This effect is one of the multiple manifestions of bubble deformations discussed in Sec. 7.

6.2. Magnetic resonance

A high degree of spin polarization is a prerequisite for sensitive magnetic resonance experiments. Magnetic resonance on electron bubbles had been previously studied in condensed helium (for a partial review of those studies see e.g. [2]) and in those experiments the electrons were polarized using the Boltzmann factor in a strong external magnetic field. To our knowledge this polarization technique has never been applied to atomic defects in condensed helium, for which the creation of polarization by optical pumping is orders of magnitude more efficient (cf Sec. 6.1). The optical properties of a polarized atomic medium depend on the orientation of the spin polarization with respect to the light polarization. In this way the spin depolarization by transverse fields (Hanle effect), by resonant oscillating fields (magnetic resonance) or by crystalline fields and gradients (zero field resonance) can be detected by optical means. In the simplest arrangement, the laser beam used for the creation of the polarization by optical pumping can be used to detect the alterations of that polarization arising from interactions with external fields. This is the very essence of the powerful method

of ODMR, which not only allows the creation of a large degree of spin polarization but also its highly efficient detection in dilute atomic samples. Most spin related experiments on alkali atoms in condensed helium were carried out using the ODMR technique.

The optical pumping process produces population imbalances, i.e., spin polarization $\langle F_z \rangle_{F=3,4}$ in both hyperfine levels of the ground state. Due to the nuclear magnetic moment, the gyromagnetic ratios of both states differ slightly in magnitude, in addition to having opposite signs, and the corresponding Zeeman splittings will be slightly different. As a consequence, the magnetic resonance transitions between Zeeman sublevels in the $F = 3$ and $F = 4$ states will occur at slightly different frequencies. Since the probing laser interacts simultaneously with both hyperfine states one can observe both states in a single scan of the rf frequency (Fig. 12,*a*).

As mentioned above, Kinoshita et al. [52] were the first to observe magnetic resonance on alkalis implanted in superfluid helium using the ODMR technique. The longer relaxation time obtained in the cubic phase of solid helium allowed us to observe magnetic resonance lines in such matrices with a width (HWHM) of only 10 Hz [58]. We took advantage of these narrow lines to build an optically pumped magnetometer in the M_x geometry [58] and were able to demonstrate a magnetometric sensitivity of 2.6 pT for an integration time of 1 second.

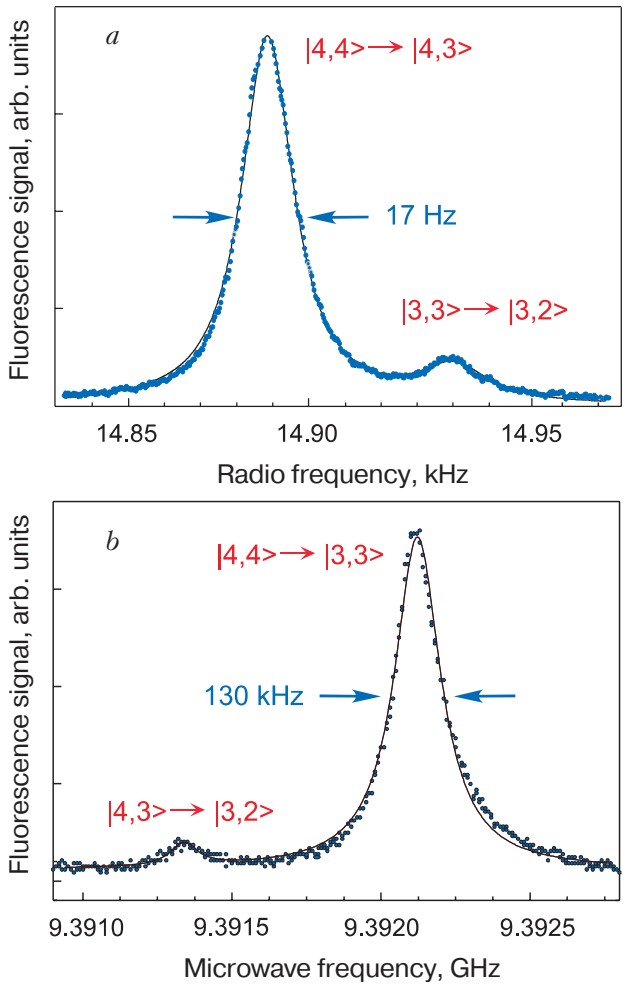

Fig. 12. Intramultiplet (*a*) and intermultiplet (*b*) magnetic resonance spectra of Cs in bcc ^{4}He. *a* and *b* refer to the transitions *A* and *B* shown in Fig. 15. Note the difference of the linewidths in the two cases.

As discussed in Sec. 5, rubidium emits fluorescence in liquid helium, but the fluorescence intensity is strongly quenched when the helium pressure is increased and it was long believed that Rb would not fluoresce at all in solid helium. It is only recently that we could observe a faint fluorescence from Rb in solid helium [18]. The relatively strong fluorescence of Rb in superfluid matrices allowed Kinoshita et al. [52] to observe ODMR signals in that phase. To measure magnetic resonance from Rb in solid helium we used the fact that Rb still has resonant optical absorption, despite the fact that its deexcitation is mainly radiationless in the atomic channel. Because of the low optical thickness (10^{-5}–10^{-4}) the absorption is difficult to detect. Using the M_x variant (Fig. 13) of ODMR, in which the magnetic resonance process induces a modulation of the transmitted intensity at the rf frequency, we were able to detect magnetic resonance signals from rubidium atoms embedded in the bcc phase of solid helium [59]. In that experiment, low-frequency intensity noise was rejected by phase sensitive lock-in detection, which allowed us to extract the weak signal modulation due to the resonantly driven spin precession. In this way we have shown that the helium matrix does not affect the Landé g_J-factors of ^{85}Rb, ^{87}Rb, and ^{133}Cs at a level of $2 \cdot 10^{-4}$, and that the g_I factors coincide at least at the level of 10% with those of free atoms [59]. The study also revealed that the optical pumping process in Rb is of the depopulation type, in which spin pola-

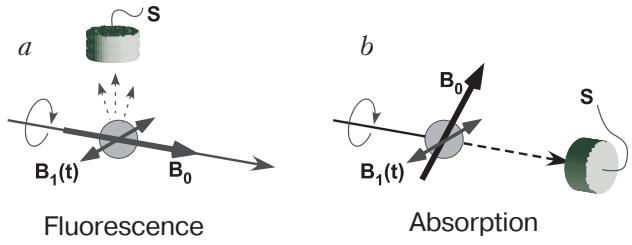

Fig. 13. Geometries for optically detected magnetic resonance spectroscopy with static (B_0) and oscillating (B_1, rf or microwave) magnetic fields: (*a*) M_z in which the fluorescence shows a resonant DC change when the Larmor frequency coincides with the oscillating field frequency, and (*b*) M_x geometry, in which the transmitted light intensity is modulated at the frequency of the oscillating field.

rization in the excited state is destroyed by the matrix interaction, whereas in cesium, repopulation is the dominant mechanism. This is a direct consequence of the fact that the excited Rb state decays via an intermediate exciplex state to the ground state, a process in which spin polarization is destroyed. In principle it should therefore also be possible to monitor the ground state spin polarization via the far red detuned emission of exciplex fluorescence, although this has not yet been attempted.

6.3. Relaxation times

Longitudinal relaxation. In our first experiments on optically pumped cesium in solid helium we have determined T_1, i.e., the longitudinal relaxation time of the spin polarization, using the method of «relaxation in the dark» [54]. We found T_1 to vary in the range of 1–2 seconds when the external holding field was varied in the range of 10 nT to 100 μT [57]. In the original optical pumping study [52] in He II, the T_1 time was not measured. Only recently did Furukawa et al. [60] determine the T_1 time of spin polarized cesium in *superfluid* helium. In that experiment great care was taken to suppress contributions from the loss of atoms due to convection and a lower bound of $T_1 = 2.24(19)$ s was found for the longitudinal relaxation time. The T_1 times of 1 or 2 seconds observed with cesium atoms in solid [54] and in superfluid [60] helium, respectively, are longer than the ones observed in vapor cells in which inert buffer gases or special surface coatings are used to prevent depolarizing collisions with the cell walls.

The question as to why the T_1 times in condensed helium are only 1–2 seconds and not orders of magnitude longer has not yet found a quantitative answer. It is known that static quadrupolar deformations of the atomic bubbles in hcp matrices depolarize the atoms on a time scale of a few 10 μs (cf. Sec. 7). Because of its quantum nature, the spherical bubble interface in the bcc phase undergoes large zero point oscillations which can be decomposed into oscillations of different multipole orders, and the atomic spins will couple to the quadrupolar deformations. Bubble surface oscillation frequencies can be estimated to lie in the gigahertz range and are much faster than the depolarization rate due to a deformed bubble. In that case the depolarizing effect of a given instantaneous deformed bubble configuration will not be very effective, and one has to apply the theory of motional narrowing [61] to infer the effective lifetime of the spin polarization.

Transverse relaxation. Transverse relaxation times are more relevant for practical applications as they determine the width of magnetic resonance lines. They can either be inferred from the widths of these lines, from free induction decay signals, or from spin echo experiments. In the first experiments on optically pumped rubidium and cesium atoms in superfluid helium, Kinoshita et al. [52] observed magnetic resonance linewidths on the order of 50 μT which correspond to a spin coherence relaxation time (T_2 time) on the order of 1 μs. They found that strong convection currents in He II carried the atoms out of the observation volume. The large rf intensity required for observing the spin flip transitions under those conditions is at the origin of the observed relatively short coherence times.

In solid helium matrices the atomic diffusion time is orders of magnitude longer than the observation times realized in liquid helium and the magnetic resonance lines were expected to be substantially narrower in such matrices. In 1995 we reported the first observation of magnetic resonance signals from cesium atoms trapped in the isotropic bcc phase of solid ^{4}He [54]. In those experiments we recorded level crossing signals (ground state Hanle effect) in longitudinal and transverse fields as well as magnetic resonance lines [54]. The widths of both the Hanle resonances and the magnetic resonances (extrapolated to low rf power) gave consistent values of 300 nT, which corresponds to an effective T_2 time of 150 μs. Although more than two orders of magnitude larger than the corresponding T_2 times in superfluid helium, those values were almost four orders of magnitude lower than the T_1 time in solid helium. After improving our apparatus we have redetermined the T_2 times in 1996 [58] using the technique of «FID (free induction decay) in the dark» and found a lower limit $T_2 > 108(3)$ ms for the transverse spin relaxation time, which is only one order of magnitude below the T_1 time. There is no *a priori* reason why the T_1 and T_2 times of dilute Cs samples in condensed helium should be significantly different. The T_2 value of 108 ms can be explained by a magnetic field inhomogeneity on the order of 10^{-7}. Although a spin echo experiment would be the technique of choice for measuring the intrinsic T_2 time, such an experiment was not yet carried out.

6.4. Multiphoton transitions in the ground state of Cs in bcc ^{4}He

The normal magnetic resonance transition is a $\Delta M = \pm 1$ magnetic dipole transition, in which one rf photon of a given helicity is absorbed between adjacent Zeeman sublevels . The selection rules imply that resonances between states with magnetic quantum numbers differing by $\Delta M = \pm N$ can also be driven by the simultaneous absorption of N photons of the same helicity. In the case of a linear Zeeman splitting of the different M levels all these processes are resonant at

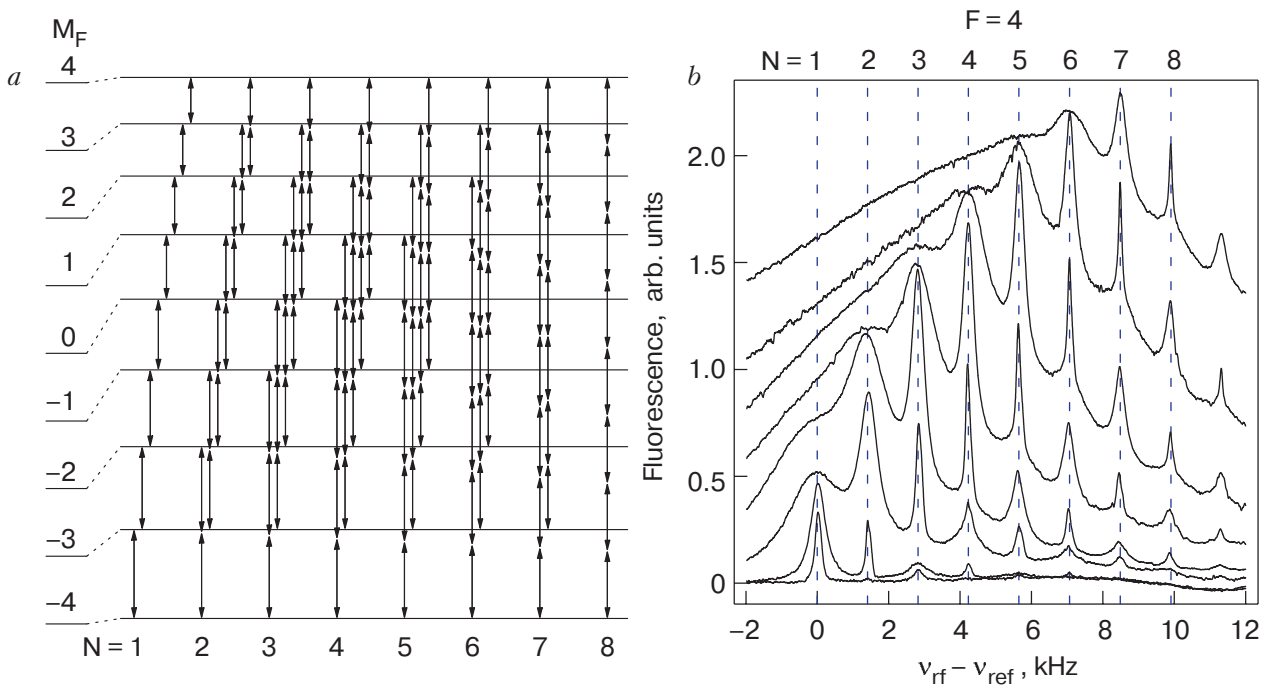

Fig. 14. (*a*) Possible transitions involving absorption of N rf photons between the Zeeman sublevels of the $F = 4$ ground state of the Cs atom, in a magnetic field which produces a linear and quadratic Zeeman shift. (*b*) Magnetic resonance spectra showing the multiphoton transitions of (*a*). The rf power increases from the bottom to the top.

the same frequency, i.e., when the rf frequency ω_{rf} coincides with the Larmor frequency ω_0. When one increases the magnetic field, the quadratic Zeeman effect splits the magnetic levels of a state with angular momentum F into $2F + 1$ components between which $2F$ individual one-photon resonances can be driven (Fig. 14,*a*) which form a spectrum of $2F$ equally spaced lines (Fig. 14,*b*, bottom). This forms the basis for observing the higher order transitions. Increasing the rf power the $2F - 1$ individual two-photon resonances appear next as narrow peaks located at the midpoints between the power broadened and saturated one-photon resonances (Fig. 14,*a*). This behavior continues when the rf power is further increased, and broadens/saturates the two-photon resonances, after which $2F - 2$ individual three-photon resonances appear, this time again at the positions of the one photon resonances. The procedure repeats until the highest order process, i.e., a transition between the levels $M = -F$ and $M = F$ involving the absorption of $2F$ photons is reached. The long spin relaxation times and the narrow magnetic resonance lines of cesium in bcc solid helium make this sample well suited for the study of those processes. In an experimental study [62] we have indeed observed (Fig. 14,*b*) all multiphoton processes in the $F = 4$ hyperfine ground state up to the process of simultaneous absorption of 8 rf photons (narrowest line in top spectrum of Fig. 14,*b*). In a subsequent detailed theoretical analysis we have investigated the influence of different relaxation mechanisms on the shape of these multiphoton spectra [63].

6.5. Hyperfine transitions

Magnetic resonance transitions can not only be driven within a given F multiplet (process A in Fig. 15), but also between the two hyperfine multiplets (process B in Fig. 15). In the free cesium atom the corresponding resonance frequency is on the order of 9.2 GHz (clock transition). We have studied this intermultiplet transition with cesium in the bcc and in

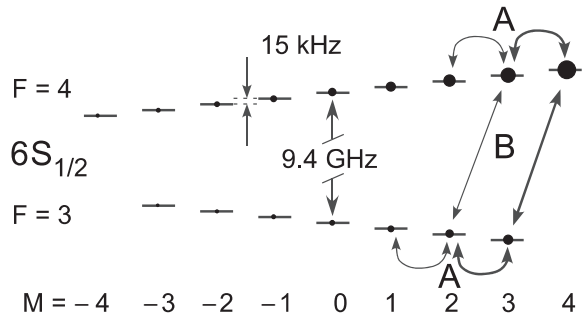

Fig. 15. Hyperfine-Zeeman structure of the ground state of cesium in a static magnetic field of 4.3 μT with intramultiplet (*A*) and intermultiplet (*B*) magnetic resonance transitions observed in solid helium. The solid dots represent relative sublevel populations achieved by optical pumping with circularly polarized light.

the hcp phase of ^{4}He [64]. In bcc phase we found that the transition is blue shifted by approximately 200 MHz with respect to the transition in the free atom (see Fig. 18,*b*) and that this shift increases with pressure at a rate of ~ 1.4 MHz/bar. The blue shift can be explained by the fact that the He matrix compresses the wave function of the valence electron, so that $|\Psi_{6S_{1/2}}(R=0)|^2$ and thus the hyperfine coupling constant of the Fermi contact interaction increases. The quantitative value of the shift and its pressure dependence can be predicted in a satisfactory way by the bubble model [20,65]. The linewidth of the hyperfine transition in bcc ^{4}He was found to be on the order of 100 kHz, i.e., 10^4 times larger than the width of the intermultiplet magnetic resonance transitions discussed above.

6.6. The Stark effect of Cs *in bcc* ^{4}He

Recently we have investigated the effect of a static electric field on the properties of the cesium ground state [66]. The motivation for this study was twofold: firstly, the quadratic Stark effect constitutes a background signal which may induce systematic errors in experiments searching for electric dipole moments, and secondly, there has been a 40-year-old discrepancy between theoretical and experimental values of the tensor polarizability of the cesium ground state. The energy of the $6S_{1/2}$ ground state magnetic sublevel $|F,M\rangle$ is shifted by a static external electric field $\mathbb{E}$ according to

$$\Delta E(6S_{1/2},F,M) = -\frac{1}{2}\alpha(6S_{1/2},F,M)\mathbb{E}^2\,, \quad (4)$$

where the polarizability $\alpha(6S_{1/2},F,M)$ is given by

$$\alpha(6S_{1/2},F,M) = \\ = \alpha_0^{(2)} + \alpha_0^{(3)}(F) + \alpha_2^{(3)}(F)\frac{3M^2 - F(F+1)}{I(2I+1)}\,. \quad (5)$$

In Eq. (5) one distinguishes three contributions, viz., the scalar polarizability, $\alpha_0^{(2)}$, which arises in second order perturbation theory and which leads to a common (i.e., F and M independent) shift of all levels, an F-dependent scalar polarizability, $\alpha_0^{(3)}$, which arises in third order perturbation theory (involving the hyperfine interaction), and a third order tensor polarizability, $\alpha_2^{(3)}$, which provides F and M dependent level shifts. For cesium, the values of the three contributions are in the ratio $\alpha_0^{(2)}:\alpha_0^{(3)}:\alpha_2^{(3)} \approx 1:10^{-5}:10^{-7}$. It was the tiny tensor polarizability $\alpha_2^{(3)}$ which was at the center of our interest. A few years ago we had remeasured $\alpha_2^{(3)}$ in a thermal atomic beam and had confirmed earlier experimental results [67]. Because of the narrow magnetic resonance lines obtained with Cs in bcc ^{4}He, an ODMR measurement in an external field was the method of choice for this study.

For the Stark shift experiments we equipped the pressure cell as described in Sec. 4.3. By using a set of mirrors, we could easily switch between the M_x and the M_z configurations (Fig. 13) by a simple beam translation (Fig. 5,*b*).

In the strongly polarized ground state, the magnetic resonance is dominated by the $|F=4,M=4\rangle \to |4,3\rangle$ transition and the differential Stark shift of the two involved levels appears as a shift of the magnetic resonance frequency proportional to $\mathbb{E}^2$ due to the $\alpha_2^{(3)}(4)$ contribution of Eq. (5). The inset in Fig. 16 illustrates the magnetic resonance shift in an electric field as measured in the M_z geometry (Fig. 13,*a*). Because of an unexplained drift of the magnetic resonance frequency, the measurement of the Stark shift from a series of individual scans in different electric fields yielded a large scattering of the data points. We have therefore used a faster recording method which consisted of locking the rf frequency to the Larmor frequency [58] using feedback in the M_x configuration (Fig. 13,*b*). This has allowed us the direct, and therefore faster, recording of the Larmor frequency changes upon application of the electric field. The resulting (quadratic) electric field dependence of the Larmor frequency is shown in Fig. 16, from which one can extract the tensor polarizability $\alpha_2^{(3)}$. The result $\alpha_2^{(3)}(F=4) = -3.31(30)\cdot 10^{-2}\,\mathrm{Hz/(kV/cm)^2}$ is in good agreement with the earlier atomic beam experiments (see [67] and references therein). In parallel we reanalyzed the theoretical calculation of the Stark

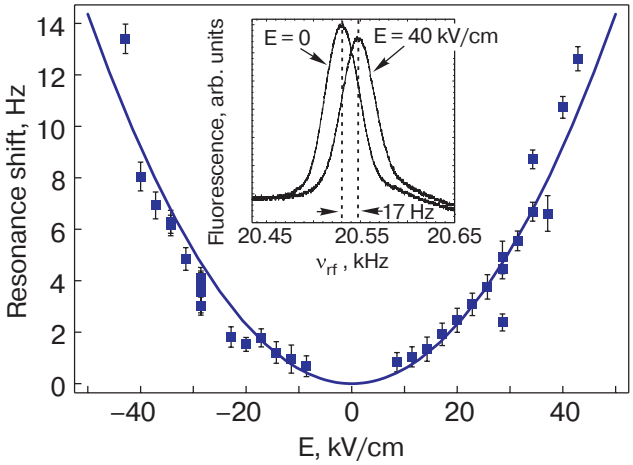

Fig. 16. Quadratic Stark shift of the magnetic resonance frequency in a magnetic field of 6 μT recorded with a feedback lock of the rf frequency to the center of the magnetic resonance line in the M_x geometry. The inset shows a particular value of the Stark shift recorded in the rf scanning mode.

shift, thereby identifying terms omitted in earlier treatments as well as a sign error. The numerical evaluation of those terms has allowed us to reconcile experimental and theoretical values of $\alpha_2^{(3)}$ after 40 years of discrepancy [66,68].

7. Deformed bubbles

As discussed in Sec. 5, the spherical bubble model described in Sec. 3 has proven to be very effective for describing atomic absorption and emission spectra in an isotropic environment such as the liquid or bcc phase of solid He. Here we want to address the extension of the model to bubbles with static or dynamic deformations. The uniaxial hcp phase of solid helium has anisotropic elastic constants, so that the repulsive force exerted by the dopant is counteracted by anisotropic restoring forces, leading to deformed bubbles. As the anisotropies are small, it is reasonable to describe the deformation in lowest order by a quadrupolar shape which can be parametrized as

$$\frac{R_b(\vartheta)}{R_0} = 1 + \beta(3\cos^2\vartheta - 1) = P_0(\cos\theta) + 2\beta P_2(\cos\theta)\,, \tag{6}$$

where the $P_l(\cos\theta)$ are Legendre polynomials. The bubble radius parameter R_b of Eq. (2) depends on the azimuthal angle ϑ measured with respect to the bubble axis, and β characterizes the bubble deformation. In a similar way as described in Sec. 3, the three parameters R_0, α, and β can be found by minimizing the defect energy. Besides these static deformations in the hcp phase one also has to consider dynamical deformations (in both phases). The latter are due to the zero-point fluctuations of the helium atoms on the bubble interface which may be expressed as the sum over (uncorrelated) shape oscillations of different multipole orders.

Different effects have been identified which can be traced back to dynamic and static deformations. Dynamic quadrupole deformations (oscillations) were first considered in [69] for explaining the characteristic doubly-shaped contour of the D_2 excitation line of Rb and Cs in superfluid He (see also Fig. 6,*b*). Such anisotropic oscillations split the absorption line due to a dynamic Jahn–Teller effect. A more general approach including monopole (breathing), dipole, and quadrupole modes of the bubble oscillations was applied in [70,71] for the analysis of the excitation spectra of Yb^+ ions and Ca atoms in liquid helium. As mentioned above in Sec. 6.3 quadrupolar oscillations may also be responsible for the finite, but rather long spin relaxation time of alkali atoms in superfluid and bcc matrices, and finally the symmetric monopole (breathing mode) oscillations were suggested to explain the relatively large width of the hyperfine magnetic resonance transition [20,64] (Sec. 6.5).

Figure 17 gives an overview of bubble effects when going, first from vacuum to spherical bubbles and then to bubbles with a static deformation. The effect of a spherical bubble on the optical transitions was discussed in detail above. Here we address the additional effects induced by a (small) static quadrupolar bubble deformation superimposed on the spherical bubble as it arises when going from bcc to hcp ^{4}He. As shown in Fig. 17 the deformation affects the optical transitions, the hyperfine structure and the Zeeman structure of the individual hyperfine levels. When going from the bcc to the hcp phase by increasing the helium pressure at constant temperature, the

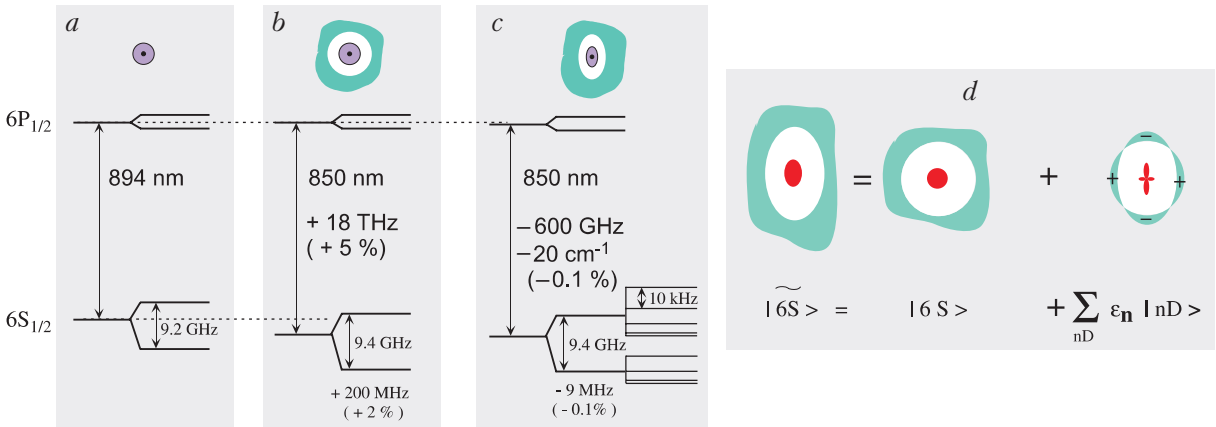

Fig. 17. Wavelength of the D_1 transition and hyperfine frequency of the free Cs atom (*a*); effects of the spherical bubble in bcc ^{4}He on the optical and microwave transitions (*b*); additional perturbations of the optical, the hyperfine and the Zeeman transitions due to deformed bubbles (*c*); the deformed bubble seen as a spherical bubble with a quadrupolar change of He density at its interface and the corresponding perturbed ground state of Cs interpreted as an *S* orbital with a *D* orbital admixture (*d*).

atomic density rises and one would naively expect that any line shifts induced by the symmetric bubble in bcc phase would further increase at the phase transition. In this sense the optical absorption frequency and the hyperfine transition frequency, which are both shifted to the blue by the spherical bubble, would experience a further blue shift. However, the experiments have revealed that both frequencies jump to the red at the bcc → hcp phase transition, after which they move again towards the blue upon a further pressure increase (Figs. 7 and 18,*b*).

The theoretical treatment of deformation induced effects starts from the interpretation of a bubble deformation in terms of a prolate (oblate) quadrupolar change of the surrounding helium density: He atoms are added (removed) along one direction and removed (added) along the orthogonal directions. For symmetry reasons the corresponding perturbation operator will have the form

$$V_{\text{def bub}} = f(r)P_2(\theta)\,, \tag{7}$$

which has the symmetry of a second rank tensor that perturbs the $6S$ state by admixtures of nD states according to

$$|\widetilde{6S}\rangle = \frac{|6S\rangle + \sum_n \varepsilon_n |nD\rangle}{\sqrt{1+\sum_n \varepsilon_n^2}}\,, \tag{8}$$

where the S–D mixing coefficients ε_n are given by

$$\varepsilon_n = \frac{\langle nD|V_{\text{def bub}}|6S\rangle}{E_{6S} - E_{nD}}\,. \tag{9}$$

The energy minimization procedure applied to the (deformed) bubble model then establishes a relation between the bubble deformation parameter β and the S–D mixing coefficients ε_n. In this way we have interpreted the hyperfine frequency red shift at the bcc → hcp transition as originating from a loss of the S character of the ground state wave function according to Eq. (8). This has allowed us [56] to infer a $6S$–$5D$ mixing coefficient of 3% and from that a bubble deformation parameter of β = 6–7%.

For the explanation of the observed red shift of the D_1 absorption line [20] we propose the following qualitative explanation. The spherical $6S$ ground state does not fit into the deformed bubble and the interaction $V_{\text{def bub}}$ increases its energy. At the same time the spherically symmetric excited $6P_{1/2}$ state is mixed by $V_{\text{def bub}}$ with the nearby $6P_{3/2}$ state to produce a deformed state, which has a better fit to the bubble shape, so that the energy increase of the exited state is smaller than the one of the ground state. As a result the transition wavelength becomes red-shifted. A further increase in pressure tends to render the bubble more spherical, hence the ensuing correlated blue shift of the transition frequencies. We are currently working on the quantitative investigation of this hypothesis.

Finally, we discuss the most remarkable effect that deformed bubbles have on the intramultiplet Zeeman transitions (transitions A in Fig. 15). In Fig. 18,*a* we compare the ultranarrow magnetic resonance lines obtained with Cs in the bcc phase to the extremely broad magnetic resonance spectrum observed in the hcp phase under otherwise identical conditions. The spectrum is broadened by more than three orders of magnitude and shows a rich substructure which indicates a lifting of the Zeeman degeneracy induced by the bubble deformation. The validity of this assumption has been demonstrated in a convincing way by the obser-

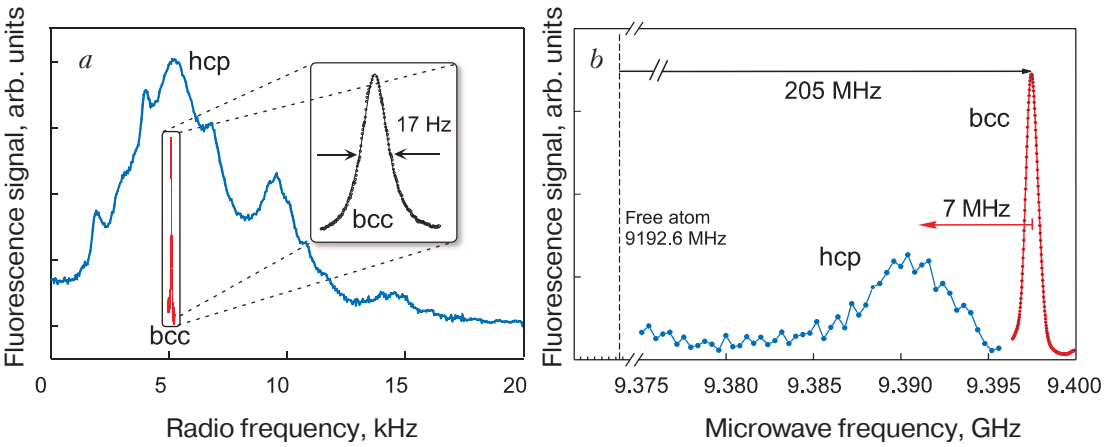

Fig. 18. Comparison of intramultiplet (Zeeman) magnetic resonance spectrum of cesium in bcc and hcp ^{4}He (*a*). Comparison of intermultiplet (hyperfine) magnetic resonance spectrum of cesium in bcc and hcp ^{4}He. Both spectra were recorded in a single scan in which the phase transition was induced by a pressure change during the scan between the two resonances (*b*).

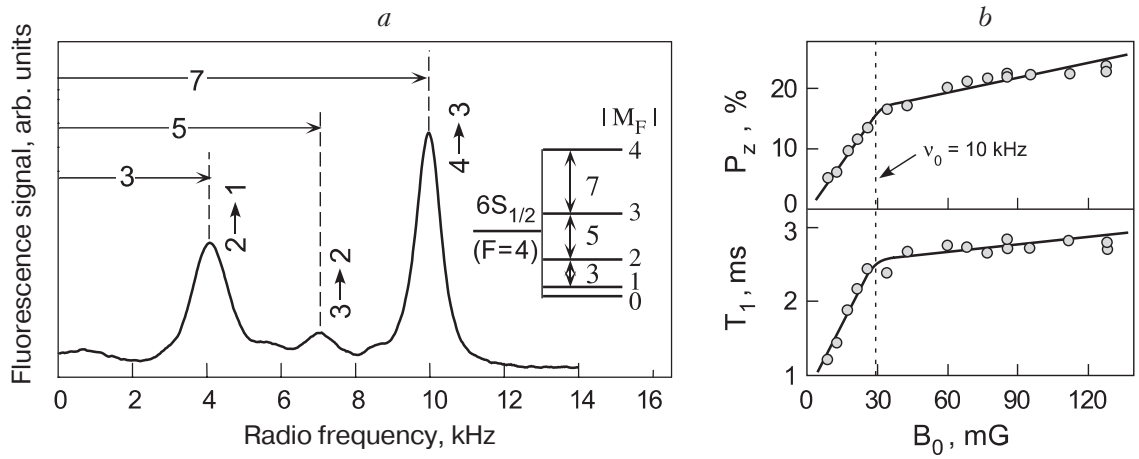

Fig. 19. Zero field magnetic resonance spectrum in the $F = 4$ ground state of cesium trapped in hcp ^{4}He. The inset shows the level structure expected from a third order perturbation by quadrupolar bubble deformations. The lines are slightly rf power broadened and the weaker lines at the midpoints between the main lines correspond to $\Delta M = 2$ transitions induced by the absorption of 2 rf photons. The magnetic resonance spectrum shown in Fig. 18,*a* can be understood as the Zeeman splitting of the spectrum shown here (*a*). Spin polarization (top) and longitudinal relaxation rate (bottom) as a function of the magnetic field. Decoupling occurs at a Larmor frequency of 10 kHz, which coincide with the rightmost resonance of the zero field spectrum (*b*).

vation of a zero magnetic field magnetic resonance spectrum (Fig. 19,*a*) recorded with the arrangement of Fig. 13,*a*, with $B_0 = 0$. As shown in the inset, the main features of the spectrum can be understood as resulting from a quadrupolar shift of the energies of the levels $|6S_{1/2}, F, M\rangle$ according to

$$\Delta\nu_{F,M} = \nu_Q[3M^2 - F(F+1)]\,. \qquad (10)$$

In the Fig. 19,*b* we show the dependence of the degree of spin polarization $P_z = \langle J_z \rangle$ and of the longitudinal relaxation time T_1 on the magnetic holding field. Both quantities are much smaller than in bcc ^{4}He due to the faster spin relaxation experienced in hcp ^{4}He. In a low magnetic field, the cesium spin couples to the bubble axis and only its projection onto this axis is conserved. The maximal energy of the coupling may be estimated from Fig. 19,*a* to be on the order of 10 kHz. Since the orientations of the bubble axes in space are most probably distributed randomly (polycristalline sample) an effective spin depolarization is generated. In very large magnetic fields the spin couples to the magnetic field and its projection along the field becomes the conserved quantity. In this sense the magnetic field dependencies shown in the Fig. 19,*b* can be interpreted as a magnetic field induced decoupling of the spins from their interaction with the deformed bubbles. The kinks in these dependencies mark the intermediate region between the discussed extreme cases, and the fact that the kinks occur at a Larmor frequency of ≈ 10 kHz (in accordance with the highest energy feature of the zero-field magnetic resonance spectrum Fig. 19,*a*) gives further support to this interpretation. Note that this view is analogous to the well-known Breit–Rabi problem in which the magnetic field decouples pairs of angular momenta from their mutual (fine or hyperfine) interaction in low fields.

Naively one might expect that Eq. (10) represents just the eigenvalues of the interaction $V_{\text{def bub}}$ (Eq. (7)). However the matrix elements $\langle 6S_{1/2}|V_{\text{def bub}}|6S_{1/2}\rangle$ vanish as $V_{\text{def bub}}$ acts only in the space of orbital variables. This is similar to the quadratic Stark effect due to the perturbation $V_{\text{St}} = -ez\,\mathbb{E} \propto rP_1(\cos\theta)$ which does not lift the Zeeman degeneracies in the first and second order. However, it is known [72] that the second rank tensor part of the third order interaction $T_0^{(2)}(\text{Stark}) = [V_{\text{St}} \otimes H_{\text{hf}} \otimes V_{\text{St}}]_0^{(2)}$ produces a quadrupolar lifting of the Zeeman degeneracies in $S_{1/2}$ state. In a similar way one can show that the eigenenergies of Eq. (10) correspond to the expectation values of the second rank operator

$$T_0^{(2)}(\text{def bub}) = [V_{\text{def bub}} \otimes H_{\text{hf}} \otimes V_{\text{def bub}}]_0^{(2)}\,. \qquad (11)$$

The coupling of the atomic spin, or rather the atomic magnetic moment, to the axis of a nonspherical bubble is very weak with an interaction energy on the order of 10 kHz, i.e., some $3\cdot10^{-7}$ cm^{-1}. The weakness may be appreciated by comparing it to the coupling of nuclear quadrupole moments to electric field gradients in uniaxial crystals, which are typically measured in megahertz.

8. Search for an electric dipole moment of the electron

Our original motivation for investigating alkali atoms in condensed helium matrices was the hope that such samples might be used for the search of a permanent electric dipole moment (EDM) of the electron [51,73–75]. An EDM violates the discrete symmetries of parity and time reversal invariance and the existence of such a moment would advance modern particle physics theories beyond their presently best description in terms of the standard model. EDM experiments are carried out with neutral species involving an unpaired electron and aim at detecting a shift of a magnetic resonance frequency proportional to the strength of an externally applied electric field. Sensitive experiments therefore call for narrow magnetic resonance lines, i.e., long spin relaxation times and environments which can sustain large electric fields. It was speculated [51] that alkali atoms in solid helium may fulfill the former condition, while it was known that pure liquid or solid helium has a very high dielectric strength. As discussed above it was later found that long spin coherence times are impossible to realize in He II, but it was subsequently shown that one can indeed observe extremely narrow magnetic resonance lines with a good signal/noise ratio with Cs and Rb in solid helium.

After a decade of efforts towards an EDM experiment with cesium in bcc ^{4}He we have now reached the conclusion that it is not possible to realize an experiment which is competitive to other past and ongoing alternative approaches. This conclusion is based on multiple reasons. Although the combination of magnetic resonance linewidth and signal/noise ratio are comparable to what can be reached in thermal atomic beams, we found recently that the maximum electric field that a doped sample can hold is on the order of 50 kV/cm, which is more than a factor of two less than the field used in the Tl beam experiment which has produced the currently lowest upper limit on the electron EDM [76]. We have also found that the magnetic resonance frequency shows a slow drift (about 2 mHz/s) in time [20,66]. The origin of the drift is not clear, although we have shown that it is not correlated with magnetic field drifts in our 3-fold shield nor with pressure or temperature changes of the crystal. Such a drift is of course detrimental for EDM expriments in which one wants to compare magnetic resonance frequencies in a geometry in which $\mathbb{E}$ is parallel to B_0 with one where $\mathbb{E}$ is antiparallel to B_0. In Sec. 7 we have shown that a bubble deformation on the order of 6–7% causes an interaction energy of 10 kHz. The present upper limit of the electron EDM of 10^{-27} e·cm corresponds to an EDM of the cesium atom of approximately 10^{-25} e·cm, which, in an electric field of 50 kV/cm, induces an electric Larmor frequency dE/h of 1 μHz. In order not to be perturbed by bubble deformations the latter have to be stable at a level of $\beta < 10^{-6}$, when assuming a quadratic relation between the bubble deformation and the corresponding shift of the Zeeman levels (see Eq. (11)). In order to avoid systematic effects related to bubble deformations, one has to ascertain that any deformation of the 1 nm sized bubbles correlated with the direction of the electric field is less than 10^{-13} cm. At present we have no idea how to achieve such precision.

Besides these fundamental and technical limitations there are also practical limitations which have forced us to abandon the EDM related branch of our research. Successful EDM experiments require a long data integration time in order to reach the required statistical sensitivity and for performing control measurements of systematic effects. Efficient experiments thus need a highly reliable apparatus, in which most of the data acquisition can be automatized, a goal which is hard to realize with the experiments on doped helium crystals. The helium holding time of the cryostat equipped for Stark spectroscopy is on the order of 2 days, out of which typically 10 hours can be used for actual data taking. The present system does not allow a refilling of the helium bath without bringing the bath up to 4 K and destroying the crystal. Despite many efforts in the development of low temperature and magnetic resonance compatible sealing techniques for the windows and the different feedthroughs of the cell [20] superleaks which manifest only at the cryogenic temperatures appear frequently following thermal cycling of the cell. Moreover, the reproducibility of the signal quality in each newly grown and doped crystal is another unsolved issue. All of these features make the experiments on doped crystals very demanding and far from allowing their automatization. Last, but not least we mention the recent trend to move from paramagnetic atoms to paramagnetic molecules for searching an electron EDM.

In polar paramagnetic molecules with one heavy atom (such as YbF or PbO) whose axes are aligned by an external field $\mathbb{E}_{\text{ext}}$ the electron experiences an internal electric field $\mathbb{E}_{\text{int}}$ which is up to five orders of magnitude larger than $\mathbb{E}_{\text{ext}}$ [77]. This large enhancement factor, compared to atoms makes such samples the most promising candidates to search for the electron EDM.

9. Concluding remarks

Starting from the initial proposal by Sergei Kanorsky from the Lebedev Physical Institute in Mos-

cow to use heavy paramagnetic atoms embedded in superfluid helium in an alternative experiment to search for a permanent electric dipole moment of the electron we have initiated in the early 1990's a related low temperature experiment in the laboratory of T.W. Hänsch at the Max-Planck-Institute for Quantum Optics in Garching (Germany). Today, 15 years later, we have reached the conclusion that such EDM experiments are not feasible with the present day technology and knowledge. However, we may claim that our efforts regarding the many aspects of such a difficult experiment have been quite fruitful in the sense that they have provided a wealth of information in the formerly unexplored field of solid helium matrix isolation spectroscopy. The present review has given an account of these different facets. Many unexpected features were discovered and extensions of the basic atomic bubble model were able to explain most of them. Because of lack of manpower, we were not able to pursue in depth many of the interesting and promising side roads which have opened up, such as the study of the exciplex lifetimes and the recently observed quenching of molecular excited states. Nonetheless, many questions could be answered such as the mystery about the quenching of fluorescence from the lighter alkalis by the discovery of exciplexes, the long standing discrepancy between experiment and theory of tensor polarizabilities, and insights into bubble deformation induced effects.

It is also interesting to note the intimate relation of the present studies with the field of doped helium nanoclusters which has risen, in parallel to our activities, over the past decade. In particular the recent discovery of exciplex spectra as well as of homo- and heteronuclear dimers in solid helium has further connected the two fields.

The current difficult funding situation makes our own future in the field of sHeMIS uncertain and the time may have come to pass the sHeMIS torch to other groups. We are aware at least of one group (Ph. Jacquier and J. Dupont-Roc at LKB in Paris) who have taken up this research and are preparing a challenging experiment to measure the anapole moment of the cesium nucleus. The anapole moment is the lowest order nuclear magnetization multipole moment which violates parity but conserves time reversal invariance. It was shown by M.A. Bouchiat and C. Bouchiat [78] that an atom with an anapole moment will exhibit a linear Stark effect when placed in an environment which has a quadrupolar symmetry. Based on our discovery of quadrupolar bubble deformations it was suggested in [78] to use Cs in an *uniaxial* hcp He crystal for realizing such an anapole moment experiment.

Acknowledgements

The research work presented above is the fruit of more than a decade of experimental and theoretical efforts carried out by a number of undergraduate students, Ph. D. students, and postdocs, and with the invaluable support of mechanical and electronics technicians and engineers. All their individual contributions are acknowledged. The doctoral thesis works that have emerged from this line of research were presented by Markus Arndt [79] and Stephen Lang [80] at the Ludwig-Maximilians Universität in Munich, by Taro Eichler [81] at the Friedrich-Wilhelms-Universität in Bonn and more recently by Daniel Nettels [82], Reinhard Müller-Siebert [20] and Simone Ulzega [66] at the University of Fribourg. One of us (A.W.) acknowledges his colleague and friend Sergei Kanorsky who submitted the original EDM proposal to the Max-Planck-Institute for Quantum Optics and with whom he initiated the first heroic steps of this research. We thank Paul Knowles for his critical reading of the manuscript.

The research was funded partly by the individual host institutions and by the national funding agencies in Germany (Deutsche Forschungsgemeinschaft, DFG) and in Switzerland (Swiss National Science Foundation, SNF). We particularly acknowledge the support of SNF by the grants 21-59451.99, 20-67008.01, and 200020-103864.

1. J.P. Toennies and A.F. Vilesov, *Annu. Rev. Phys. Chem.* **49**, 1 (1998).
2. S.I. Kanorsky and A. Weis, *Optical and Magneto-optical Spectroscopy of Point Defects in Condensed Helium,* Academic Press (1998); B. Bederson and H. Walther, *Adv. in Atomic, Molecular and Optical Physics* **38**, 87.
3. R.E. Boltnev, G. Frossati, E.B. Gordon, I.N. Krushinskaya, E.A. Popov, and A. Usenko, *J. Low Temp. Phys.* **127,** 245 (2002).
4. E.P. Bernard, R.E. Boltnev, V.V. Khmelenko, V. Kiryukhin, S.I. Kiselev, and D.M. Lee, *J. Low Temp. Phys.* **134,** 133 (2004).
5. E.B. Gordon, A. Usenko, and G. Frossati, *J. Low Temp. Phys.* **130,** 15 (2003).
6. E.B. Gordon, *Fiz. Nizk. Temp.* **30**, 1009 (2004) [*Low Temp. Phys.* **30,** 756 (2004)].
7. J. Wilks, *The Properties of Liquid and Solid Helium,* Clarendon Press, Oxford (1967).
8. J. Pascale, *Phys. Rev.* **A28**, 632 (1983).
9. J. Jortner, W.R. Kestner, S.A. Rice, and M.H. Cohen, *J. Chem. Phys.* **43,** 2614 (1965).
10. S.I. Kanorsky, M. Arndt, R. Dziewior, A. Weis, and T.W. Hänsch, *Phys. Rev.* **B50**, 6296 (1994).
11. T. Kinoshita, K. Fukuda, Y. Takahashi, and T. Yabuzaki, *Phys. Rev.* **A52**, 2707 (1995).

12. S. Kanorsky, A. Weis, M. Arndt, R. Dziewior, and T. Hänsch, *Z. Phys.* **B98**, 371 (1995).
13. A.P. Hickman, W. Steets, and N.F. Lane, *Phys. Rev.* **B12,** 3705 (1975).
14. M. Arndt, R. Dziewior, S. Kanorsky, A. Weis, and T. Hänsch, *Z. Phys.* **B98**, 377 (1995).
15. H.C. van de Hulst, *Light Scattering by Small Particles,* Dover Publications, New York (1981).
16. D. Nettels, A. Hofer, P. Moroshkin, R. Müller-Siebert, S. Ulzega, and A. Weis, *Phys. Rev. Lett.* **94**, 063001 (2005).
17. P. Moroshkin, A. Hofer, D. Nettels, S. Ulzega, and A. Weis, *J. Chem. Phys.* **124,** 024511 (2006).
18. A. Hofer, P. Moroshkin, S. Ulzega, and A. Weis, *Phys. Rev.* **A74**, No 4 (2006); *arXiv:physics/0605181* (2006).
19. P. Moroshkin, A. Hofer, S. Ulzega, and A. Weis, *Phys. Rev.* **A74**, 032504 (2006).
20. R. Müller-Siebert, *Ph. D. thesis*, University of Fribourg, Switzerland (2002), unpublished.
21. S.I. Kanorsky, M. Arndt, R. Dziewior, A. Weis, and T.W. Hänsch, *Phys. Rev.* **B49,** 3645 (1994).
22. T. Kinoshita, K. Fukuda, T. Matsuura, and T. Yabuzaki, *Phys. Rev.* **A53,** 4054 (1996).
23. J. Dupont-Roc, *Z. Phys.* **B98,** 383 (1995).
24. K. Ishikawa, A. Hatakeyama, K. Gosyono-o, S. Wada, Y. Takahashi, and T. Yabuzaki, *Phys. Rev.* **B56,** 780 (1997).
25. A.I. Golov and L.P. Mezhov-Deglin, *JETP Lett.* **56,** 514 (1992).
26. A.I. Golov and L.P. Mezhov-Deglin, *Physica* **B194–196,** 951 (1994).
27. A.I. Golov, *Z. Phys.* **B98,** 363 (1995).
28. K. Enomoto, K. Hirano, M. Kumakura, Y. Takahashi, and T. Yabuzaki, *Phys. Rev.* **A66,** 042505 (2002).
29. K. Hirano, K. Enomoto, M. Kumakura, Y. Takahashi, and T. Yabuzaki, *Phys. Rev.* **A68,** 012722 (2003).
30. K. Enomoto, K. Hirano, M. Kumakura, Y. Takahashi, and T. Yabuzaki, *Phys. Rev.* **A69,** 012501 (2004).
31. J. Reho, J. Higgins, C. Callegari, K.K. Lehmann, and G. Scoles, *J. Chem. Phys.* **113,** 9686 (2000).
32. J. Reho, J. Higgins, K.K. Lehmann, and G. Scoles, *J. Chem. Phys.* **113,** 9694 (2000).
33. F.R. Bruhl, R.A. Trasca, and W.E. Ernst, *J. Chem. Phys.* **115,** 10220 (2001).
34. C.P. Schulz, P. Claas, and F. Stienkemeier, *Phys. Rev. Lett.* **87,** 153401 (2001).
35. G. Droppelmann, O. Bünermann, C.P. Schulz, and F. Stienkemeier, *Phys. Rev. Lett.* **94,** 023402 (2004).
36. O. Bünermann, M. Mudrich, M. Weidemuller, and F. Stienkemeier, *J. Chem. Phys.* **121,** 8880 (2004).
37. J.L. Persson, Q. Hui, Z.J. Jakubek, M. Nakamura, and M. Takami, *Phys. Rev. Lett.* **76,** 1501 (1996).
38. Y. Moriwaki and N. Morita, *Eur. Phys. J.* **D5**, 53 (1999).
39. Y. Moriwaki, K. Inui, K. Kobayashi, F. Matsushima, and N. Morita, *J. Mol. Structure* **786,** 112 (2006).
40. Y. Fukuyama, Y. Moriwaki, and Y. Matsuo, *Phys. Rev.* **A69,** 042505 (2004).
41. P. Moroshkin, D. Nettels, A. Hofer, S. Ulzega, and A. Weis, *Proc. of SPIE* **6257,** 625706 (2006).
42. M. Zbiri and C. Daul, *Phys. Lett.* **A341,** 170 (2005).
43. T. Takayanagi and M. Shiga, *Phys. Chem. Chem. Phys.* **6**, 3241 (2004).
44. F. Stienkemeier, J. Higgins, W.E. Ernst, and G. Scoles, *Phys. Rev. Lett.* **74,** 3592 (1995).
45. J. Higgins, C Callegari, J. Reho, F. Stienkemeier, W.E. Ernst, M. Gutowski, and G. Scoles, *J. Phys. Chem.* **102,** 4952 (1998).
46. J. Reho, J. Higgins, and K. Lehmann, *Faraday Discuss.* **118,** 33 (2001).
47. F.R. Bruhl, R.A. Miron, and W.E. Ernst, *J. Chem. Phys.* **115,** 10275 (2001).
48. W.E. Ernst, R. Huber, S. Jiang, R. Beuc, M. Movre, and G. Pichler, *J. Chem. Phys.* **124,** 024313 (2006).
49. M. Mudrich, O. Bünermann, F. Stienkemeier, O. Dulieu, and M. Weidemuller, *Eur. Phys. J.* **D31,** 291 (2004).
50. Y. Takahashi, K. Sano, T. Kinoshita, and T. Yabuzaki, *Phys. Rev. Lett.* **71,** 1035 (1993).
51. M. Arndt, S.I. Kanorsky, A. Weis, and T.W. Hänsch, *Phys. Lett.* **A174,** 298 (1993).
52. T. Kinoshita, Y. Takahashi, and T. Yabuzaki, *Phys. Rev.* **B49,** 3648 (1994).
53. D. Budker, W. Gawlik, D.F. Kimball, S.M. Rochester, V.V. Yashchuk, and A. Weis, *Rev. Mod. Phys.* **74,** 1153 (2002).
54. M. Arndt, S.I. Kanorsky, A. Weis, and T.W. Hänsch, *Phys. Rev. Lett.* **74,** 1359 (1995).
55. S. Lang, M. Arndt, T.W. Hänsch, S.I. Kanorsky, S. Lucke, S.B. Ross, and A. Weis, *Fiz. Nizk. Temp.* **22**, 171 (1996) [*Low Temp. Phys.* **22,** 129 (1996)].
56. S. Kanorsky, S. Lang, T. Eichler, K. Winkler, and A. Weis, *Phys. Rev. Lett.* **81,** 401 (1998).
57. S. Lang, S.I. Kanorsky, T. Eichler, R. Müller-Siebert, T.W. Hänsch, and A. Weis, *Phys. Rev.* **A60,** 3867 (1999).
58. S.I. Kanorsky, S. Lang, S. Lücke, S.B. Ross, T.W. Hänsch, and A. Weis, *Phys. Rev.* **A54,** R1010 (1996).
59. T. Eichler, R. Müller-Siebert, D. Nettels, S. Kanorsky, and A. Weis, *Phys. Rev. Lett.* **88,** 123002 (2002).
60. T. Furukawa, Y. Matsuo, A. Hatekeyama, Y. Fukuyama, T. Kobayashi, H. Izumi, and T. Shimoda, *Phys. Rev. Lett.* **96,** 095301 (2006).
61. D. Pines and C.P. Slichter, *Phys. Rev.* **100,** 1014 (1955).
62. D. Nettels, R. Müller-Siebert, S. Ulzega, and A. Weis, *Appl. Phys.* **B77,** 563 (2003).
63. D. Nettels, R. Müller-Siebert, and A. Weis, *Appl. Phys.* **B77,** 753 (2003).
64. S. Lang, S. Kanorsky, M. Arndt, S.B. Ross, T.W. Hänsch, and A. Weis, *Europhys. Lett.* **30,** 233 (1995).
65. S. Kanorsky and A. Weis, in: *NATO Advanced Study Institute «Quantum Optics of Confined Systems»,* Kluwer Academic Publishers (1995).
66. S. Ulzega, *Ph. D. thesis*, University of Fribourg, Switzerland (2006), unpublished.

67. C Ospelkaus, U. Rasbach, and A. Weis, *Phys. Rev.* **A67,** 011402 (2003).
68. S. Ulzega, A. Hofer, P. Moroshkin, and A. Weis, *arXiv:physics/0609107* (2006).
69. T. Kinoshita, K. Fukuda, and T. Yabuzaki, *Phys. Rev*. **B54,** 6600 (1996).
70. Y. Moriwaki and N. Morita, *Eur. Phys. J.* **D13,** 11 (2001).
71. Y. Moriwaki and N. Morita, *Eur. Phys. J*. **D33,** 323 (2005).
72. J.R.P. Angel and P.G.H. Sandars, *Proc. R. Soc. London* **A305,** 125 (1968).
73. A. Weis, S. Kanorsky, M. Arndt, and T.W. Hänsch, *Z. Phys.* **B98,** 359 (1995).
74. A. Weis, *Hunting the Electron Electric Dipole Moment*, Plenum Press (1997), *Electron Theory and Quantum Electrodinamics — 100 Years Later*, J.P. Dowing (ed.), *Proc. of ASI* **B358**, 149.
75. A. Weis, S. Kanorsky, S. Lang, and T.W. Hänsch, *Can Atoms Trapped in Solid Helium be Used to Search for Physics Beyond the Standard Model?* Springer (1997); K. Jungmann, J. Kowalski, I. Reinhard, and F. Träger (eds.), *Atomic Physics Methods in Modern Research, Lecture Notes in Physics,* **499**, 57.
76. B.C. Regan, E.D. Commins, C.J. Schmidt, and D. DeMille, *Phys. Rev. Lett*. **88,** 071805 (2002).
77. J.J. Hudson, B.E. Sauer, M.R. Tarbutt, and E.A. Hinds, *Phys. Rev. Lett*. **89,** 023003 (2002).
78. M.A. Bouchiat and C. Bouchiat, *Eur. Phys. J*. **D15**, 5 (2001).
79. M. Arndt, *Ph. D. thesis*, Ludwig Maximilians Universität München (1995), Max-Planck-Institut für Quantenoptik, Garching, MPQ-Report 197.
80. S. Lang, *Ph. D. thesis,* Ludwig Maximilians Universität München (1997), unpublished.
81. T. Eichler, *Ph. D. thesis*, University of Bonn, Germany (2000), unpublished.
82. D. Nettels, *Ph. D. thesis*, University of Fribourg, Switzerland (2003), unpublished.